**The Thesis Committee for Ajinkya Ajit Phanse**
**Certifies that this is the approved version of the following Thesis:**

# A Low-Leakage, Low-Loss Transformer Structure for High-Frequency Applications

**APPROVED BY**
**SUPERVISING COMMITTEE:**

Alex Hanson, Supervisor

Alex Huang

# A Low-Leakage, Low-Loss Transformer Structure for High-Frequency Applications

**by**

**Ajinkya Ajit Phanse**

**Thesis**

Presented to the Faculty of the Graduate School of

The University of Texas at Austin

in Partial Fulfillment

of the Requirements

for the Degree of

**Master of Science in Engineering**

**The University of Texas at Austin**

**May 2021**

# Dedication

Dedicated to my parents.

# Acknowledgements

I would like to thank Prof. Alex Hanson for providing me an opportunity to work on this project. None of the work done in this thesis would have been possible without the continued help, guidance and all the technical and financial resources provided by him. I would also like to thank Prof. Alex Huang for reading the thesis and providing helpful comments on the same. I must also thank all the members of the 'Power Electronics and Magnetics Group' for continued support and encouragement throughout the term of the project. Particularly, I would like to thank Allen Nguyen for carrying out the layout of the printed circuit board. I would also like to thank Michael Solomentsev who was always available for providing assistance whenever required.

This work was supported by funds from Enphase.

I am grateful for all the support.

# Abstract


## A Low-Leakage, Low-Loss Transformer Structure for High-Frequency Applications

Ajinkya Ajit Phanse, MSE

The University of Texas at Austin, 2021

Supervisor: Alex Hanson

Designing transformers for HF applications with low magnetizing inductance is challenging because of increased core and copper losses and losses due to stored energy in the leakage inductance. Many converter topologies and applications cannot absorb the leakage inductance of the transformer, so designs that minimize leakage are very valuable. We propose a transformer structure which has low leakage inductance and low losses making it suitable for applications requiring energy storage transformers or coupled inductors. The transformer structure achieves near zero MMF drop across the window which results in a design with low leakage. It achieves current conduction along most of the skin of the conductors and is also suitable for high turns ratio applications because of its ability to achieve equal current sharing between paralleled turns. Because of these reasons, the transformer achieves low conduction losses without requiring the use of litz wire. Step-by-step design guidelines are proposed to achieve a roughly optimized structure and the design of a transformer with $L_{mag} = 105nH$ and 1-10 turns ratio for use in a 400W, 20-400V coupled-inductor based boost converter is presented.

## Table of Contents

List of Tables ..... x

List of Figures ..... xi

Chapter 1: Introduction ..... 1

Motivation ..... 1

Challenges in designing high frequency magnetics ..... 2

Winding loss ..... 2

Core loss ..... 4

Leakage inductance ..... 5

Achieving low leakage inductance and low loss in an HF transformer with Quasi-Distributed gaps ..... 8

Overview of the contents ..... 9

Chapter 2: A Low-Leakage, Low-Loss Transformer Structure for HF Applications ..... 10

Geometry Overview ..... 10

Reluctance model and analysis for low leakage inductance ..... 12

Leakage Inductance ..... 16

Advantages of the proposed structure ..... 20

Current distribution in the conductors – Double sided conduction ..... 20

"1 to N" transformers – Uniform current distribution in paralleled turns ..... 23

Sensitivity of $\boldsymbol{Llkg}$ to the window path reluctances ..... 25

Sensitivity of leakage inductance to vertical misalignment of turns ..... 27

Reluctance model in the presence of fringing ..... 28

Chapter 3: Design Guidelines for Optimized Design ..... 35
Simulation setup ..... 35
Balance the H-fields on either side of the winding ..... 37
Uniform distribution of B-fields in the core ..... 38
Choice of wire diameter – Vertical Fill ..... 38
Choice of window width – Horizontal Fill ..... 42
Approximately balance the core and copper losses – aspect ratio ..... 44
End Caps ..... 46
Core Material ..... 47
Chapter 4: An Example Design with $\boldsymbol{Lmag}$ =105nH, 1-10 Turns Ratio ..... 50
Design Constraints ..... 50
Design and Simulations in ANSYS-Maxwell ..... 51
Prototype construction ..... 57
Test Plan ..... 64
Finding the inductance matrix ..... 64
Determining current sharing between paralleled turns ..... 65
Determining core loss ..... 66
Performance in the coupled-inductor boost converter ..... 68
Chapter 5: Conclusion ..... 70
Appendices ..... 71
Appendix A: Simulation Setup ..... 71
Appendix B: Fringing field losses for the $\boldsymbol{Fh}$ and $\boldsymbol{Fv}$ recommendations in Chapter 3 ..... 76
Appendix C: Layout of the PCB ..... 78

Bibliography .....87

## List of Tables


Table 1 Impedance matrix comparison of the structures shown in Figure 11. Apart from the air gaps, the two transformers were otherwise similar. ..... 23

Table 2 Current distribution seen in FEA simulation in the primary winding of a 1-10 transformer with the proposed structure. ..... 24

Table 3 Current distribution seen in FEA simulation in the primary winding of a 1-10 transformer with interleaved primary and secondary windings and lumped gaps. ..... 25

Table 4 Inductance matrix values for structure in Figure 19 found using ANSYS Maxwell and reluctance model. ..... 32

Table 5 Inductance matrix values for structure in Figure 20 found using ANSYS Maxwell and reluctance model. ..... 33

Table 6 Inductance matrix values for structure in Figure 21 found using ANSYS Maxwell and reluctance model. ..... 33

Table 7 Geometry and specifications of the simulated transformer ..... 52

Table 8 Impedance matrix of the simulated transformer ..... 54

Table 9 Recommended measurements to identify parameters of the inductance matrix. ..... 65

Table 10 Current distribution among turns in the presence of $Rsense$ when 10-turn side was excited with 10A. ..... 66

## List of Figures


Figure 1 Leakage and Magnetizing inductances of commercially available energy storage transformers.....6

Figure 2 Cross-sectional view of the proposed transformer. Revolving around the z-axis produces the complete pot core structure. Red and blue circles represent the individual turns of the primary and secondary winding respectively. .....11

Figure 3 Cross-sectional view of the proposed transformer structure showing air gap reluctances ($Rg$ and $Rx$) and window reluctance ($Rw$). .....13

Figure 4 Magnetic circuit model of a n-gap transformer structure, like the one shown in Figure 3. $Rg$ and $Rx$ are airgap reluctances. $Rw$ models the reluctance of the flux path across the window. .....13

Figure 5 Cross-sectional view of the proposed transformer showing the various reluctances in the magnetic flux paths including the parasitic path, $Ra$. .....15

Figure 6 Magnetic circuit model of the structure shown in Figure 5. .....15

Figure 7 Flux flowing through the various paths in the window i.e., through $Rws$ and $Ras$ when primary was excited and secondary was open. Window path reluctances were kept constant ($Rws = Ras = 50$). Total reluctance in the core ($4Rg + 4Rx$) was also kept constant. .....16

Figure 8 Leakage inductance calculated according to the method shown in this section as a function of $Rx/(Rx + Ry)$ (a proxy for how symmetric the gaps at endcaps are) and $2(Rx + Ry)/Rg$ (a proxy for how distributed the QD gaps are). The reluctances are normalized to $Rg$. .....19

Figure 9 Leakage inductance calculated according to the method shown in this section as a function of $Rx/(Rx + Ry)$ and $Rw$. The reluctances are normalized to $Rg$. .....20
Figure 10 Current distribution seen in FEA simulation of a structure with balanced QD gaps on the center post and outer shell of the pot core structure. Transformer achieves almost uniform current distribution along the skin of the conductor .....22
Figure 11 FEA simulations of 10-10 transformers – one with the proposed structure (left) and other with a lumped gap. Impedance matrices of the two structures obtained from ANSYS Maxwell simulations are shown in Table 1 .....22
Figure 12 FEA simulations of 1-10 transformer showing the current distribution. Left – proposed structure. Right – structure with interleaved primary and secondary windings and a lumped gap. Both are designed for the same $Lmag$ and are carrying the same amount of current.....24
Figure 13 Transformer structures ($Lmag = 10\mu H$) with "balanced QD gaps" and "lumped gaps at endcaps" that were simulated in ANSYS Maxwell. .....26
Figure 14 Variation in the leakage inductance with changes in the spacing between pairs ($Rw$) as seen in the FEA simulations. .....26
Figure 15 Variation in the leakage inductance with changes in the spacing between primary and secondary conductors of the same pair ($Ra$) as seen in the FEA simulations.....27

Figure 16 Total leakage inductance (both primary and secondary leakage inductances referred to the 1-turn side) as seen in FEA simulations vs. vertical misalignment of the winding. Leakage inductance is not very sensitive to misalignments. .....28
Figure 17 Fringing field of a structure with quasi-distributed gaps. The fringing field is similar to that of an air core solenoid. Image taken from [7]. .....30
Figure 18 Magnetic circuit model of the structure shown in Figure 5 considering the local (bulging of magnetic fields in the gaps) and overall (as shown in Figure 17) fringing paths. .....31
Figure 19 Transformer with proposed QD-gapped structure ($lg = 0.11mm$ and $lx = 0.055mm$). Expected inductance matrix values according to reluctance model and ANSYS Maxwell are shown in the below table. .....32
Figure 20 Transformer with lumped gaps at end caps ($lg = 0.015mm$ and $lx = 0.625mm$). Expected inductance matrix values according to reluctance model and ANSYS Maxwell are shown in the below table. .....32
Figure 21 Transformer with unbalanced QD gaps ($lg = 0.125mm$ and $lx = 0mm$). Expected inductance matrix values according to reluctance model and ANSYS Maxwell are shown in the below table. .....33
Figure 22 Current distribution in the turns of transformers of Figure 19 and Figure 20.....34
Figure 23 Current excitations in primary and secondary windings of the simulated transformer.....36
Figure 24 Radial cross-section of the proposed transformer structure. Design parameters defining the geometry are marked.....36

Figure 25 Magnetic circuit model of a QD gapped structure with lumped reluctances of the air gaps and core pieces. [7] .....38
Figure 26 Conduction losses plotted against vertical fill when the spacing between conductor pairs ($ps$) is reduced while keeping spacing between conductors of same pair ($cs$) constant. The simulated transformer had a turns ratio of 1-10 and an approximately 1:1 aspect ratio ($rt = 12.7mm, ht = 26.6mm$) .....40
Figure 27 Conduction losses plotted against vertical fill when the spacing between conductors of the same pair ($cs$) is reduced while keeping spacing between two pairs ($ps$) constant. The simulated transformer had a turns ratio of 1-10 and an approximately 1:1 aspect ratio ($rt = 12.7mm, ht = 26.6mm$) .....41
Figure 28 Conduction losses plotted against vertical fill when the spacing between conductor pairs ($ps$) is reduced while keeping spacing between conductors of same pair ($cs$) constant. The simulated transformer had a turns ratio of 10-10 and an approximately 1:1 aspect ratio ($rt = 12.7mm, ht = 26.6mm$) .....41
Figure 29 Conduction losses plotted against vertical fill when the spacing between conductors of the same pair ($cs$) is reduced while keeping spacing between two pairs ($ps$) constant. The simulated transformer had a turns ratio of 10-10 and an approximately 1:1 aspect ratio ($rt = 12.7mm, ht = 26.6mm$) .....42

Figure 30 Power losses observed in FEA simulations for different $Fh$. Leakage inductances on the primary and that on the secondary referred to primary were used to find leakage as percentage of magnetizing inductance. The transformer had a square aspect ratio (height ≈ diameter). $Fv$ = 85%. .....43
Figure 31 Total power loss observed in FEA simulations for different $Fh$ and $Fv$. The transformer had a 3:2 aspect ratio (height ≈1.5× diameter).....44
Figure 32 Losses observed in FEA simulations of the transformer for different $Fh$. The transformer had a 3:2 aspect ratio (height ≈1.5× diameter). $Fv$ =85%. .....45
Figure 33 Total power loss observed in FEA simulations for different Aspect Ratios. All structures had a vertical fill of ≈ 85%. .....45
Figure 34 Larger B-fields (red) in the end caps at the edges of the window. .....46
Figure 35 Thicker endcaps lead to lower power losses. This, however, is at a cost of increased volume. .....47
Figure 36 Performance Factor comparison of different materials. Image taken from [10]. .....48
Figure 37 Performance Factor comparison: Material-80, Material-67 and Material-79. Image taken from [11]. .....49
Figure 38 Circuit schematic of a coupled-inductor boost converter. .....51
Figure 39 Equivalent circuit of the transformer based on the inductance matrix values obtained from ANSYS Maxwell simulation.....54
Figure 40 Balanced H-fields on the two sides of the winding. .....54
Figure 41 Current distribution in the windings. The winding maintains double sided conduction in all the turns. .....55

Figure 42 B-field in the core. Balancing the H-field in the center-post and outer-shell leads to an almost uniform distribution of B-field in the core. .....56
Figure 43 Current waveforms in the primary winding (green), secondary winding (blue) and solid loss in the winding (red). Average solid loss = 720mW.....56
Figure 44 Total core loss in the transformer (average = 403mW). Average core loss in center-post, outer-shell and endcaps was 176mW, 151mW and 75mW respectively. .....57
Figure 45 Drawing of a C-shaped piece of the outer shell that was manufactured. Eleven such pieces will be stacked (with laser cut pieces of shim stock providing the airgap spacing) to form one half of the outer shell.....58
Figure 46 Drawing of piece of the center post that was manufactured. Eleven such pieces will be stacked (with laser cut pieces of shim stock providing the airgap spacing) to form the center post.....59
Figure 47 Drawing of an endcap that was manufactured.....59
Figure 48 Winding pattern for the primary and secondary turns. .....61
Figure 49 Winding wound on a 3D printed jig. The primary has 10 paralleled turns that are interleaved with secondary (as shown in Figure 48). Each turn is glued to adjacent ones so that it maintains its shape.....62
Figure 50 Center post pieces made out of plastic being assembled. A metal rod helps in alignment. Laser cut pieces of shim stock used to provide an air gap.....62
Figure 51 Winding being inserted on the assembled center post.....63
Figure 52 Outer shell pieces being mounted on a jig. Laser cut shim stock pieces provide the airgap. .....63

Figure 53 Assembled structure was covered with multiple layers of tape to apply vertical pressure. .....64
Figure 54 Layout of the test circuit with loops highlighted. .....65
Figure 55 Core loss measurement circuitry with equivalent model of the transformer[23] .....68
Figure 56 A conventional pot core transformer (1-10 turns, $Lmag = 105nH$) built for comparison with the proposed transformer structure. .....69
Figure 57 Average B-field in the center-post as a function of time .....74
Figure 58 B-H data input to ANSYS Maxwell. .....74
Figure 59 Power loss density at different frequencies input to ANSYS Maxwell. .....75
Figure 60 Comparing core loss predictions of Improved Generalized Steinmetz Equation and ANSYS Maxwell .....75
Figure 61 Solutions to Equation 35 for various recommended $Fh$ and $Fv$ values. $Fh$ and $Fv$ combinations to the left of the red line satisfy $p < 4s$ criteria...77

# Chapter 1: Introduction

## MOTIVATION

Solid state power conversion has seen advancements on many fronts. The proliferation of Metal Oxide Semiconductor Field Effect Transistors (MOSFETs), the advent of Wide Bandgap Devices, and advancements in multi-layer ceramic capacitors have enabled steady increases in the switching frequency of the power converters. Faster switching frequencies are desirable because they lead to reduced volume of energy storage components (like capacitors and magnetics), which increases the power density of the converters. Miniaturization of power converters makes possible their proliferation in current applications and enables incorporation in new ones. Reducing the size of magnetics, however, has fundamental limitations which requires committing more research efforts to advance the state-of-the-art. Even today, it is not uncommon to find magnetics accounting for more than half of the power converter's volume.

Scaling down the size of magnetics leads to a larger reduction in the power handling capacity of the magnetic device. For example, for the same power handling capability, a larger magnetic structure would have better performance than multiple smaller magnetic structures processing the same net power [1]. Hence, magnetics faces an uphill battle to miniaturization, more so than capacitors.

While energy storage requirements decrease with frequency, both core loss and copper loss increase; nevertheless, it has been shown that magnetic components should still decrease in volume up to tens of MHz [10] so long as magnetic structures can be designed to avoid proximity effect losses.

## CHALLENGES IN DESIGNING HIGH FREQUENCY MAGNETICS

Core and copper losses, both scale up very quickly with the frequency of operation and the conventional approaches of reducing these losses either do not work well or can even lead to more harm than good at HF. For example, using wider conductors to reduce the DC resistance can significantly increase conduction losses. This is contrary to what one would expect with the knowledge of only the low frequency loss mechanisms. These increased losses at high frequencies can be attributed to the eddy currents induced in the conductor. It is thus important to understand and invest more research efforts towards mitigating high frequency loss mechanisms to allow miniaturization of the magnetics, and hence also power converters.

### Winding loss

Winding losses in a transformer increase significantly with frequency due to skin and proximity effects. The eddy currents induced in a solitary conductor tend to increase the current density at the conductor surface and reduce it in the center. The current density in the conductor drops exponentially; the characteristic length of which is called skin depth ($\delta$). Skin depth is inversely proportional to the square root of frequency. Thus, at higher frequencies the conductor experiences larger current crowding and higher effective resistance. In many cases, in a non-isolated conductor the H-field around it is not the same in magnitude. Current in the conductor crowds near the regions closest to the high H-fields. This uneven distribution of current along the skin of the conductor further increases the resistance.

Multiple papers have attempted modelling losses due to these high frequency mechanisms, and many others have proposed ways of dealing with the same. Some commonly employed methods are – interleaving the primary and secondary turns of the

transformer, using single layer windings, shaping the coils to keep them away from the fringing fields and using litz wires.

Each of the above methods, however, has certain limitations. Interleaving of windings reduces proximity effect losses by reducing the H-fields in the window. This, however, helps little in converters in which the currents in the primary and secondary windings are out of phase – like flyback converters. For converters like these and others, litz wire is a commonly employed solution to reduce proximity losses. Litz wire is formed out of hundreds of fine strands that are externally connected in parallel. These strands are twisted in a way that every strand occupies every position inside and on the surface of the wire. Because of this manner of twisting the strands, the current does not have a preference for which strand to flow through and thus flows almost uniformly across the entire cross-section of the wire and does not crowd towards the high H-field regions. While litz wires successfully reduce the proximity effect losses, each of the strands in the bundle needs to be smaller than the skin depth at the frequency of operation. So as frequencies increase, thinner and thinner strands are necessary. The cost of incorporating litz wires with very fine strands increases sharply with the frequency of operation. The diameter of 48AWG wire is $31\mu m$, which is equal to one skin depth in copper at 4.5MHz at room temperature. Manufacturing of wires thinner than 48 AWG becomes economically unviable for most applications. Because of the considerable premium that needs to be paid for litz wires, for a cost constrained design, the litz wire might become unviable much earlier than 4 MHz [17]. Thus, finding ways of reducing the proximity effect losses and making the most of solid conductors is important for enabling the power converters to operate at high frequencies efficiently and economically.

In addition to the skin and proximity effects, fringing fields near the gaps in the core also contribute to conduction losses. This effect gets worse with increase in the frequency. Some commonly employed methods to mitigate the losses from these fringing fields are – shaping the winding to keep it away from these fields or placing the entire winding away from the gap. Using a Quasi-Distributed (QD) gap instead of a single lumped gap is another way to reduce the fringing losses [2][7][23]. The QD gap drops the MMF across multiple smaller gaps leading to lower losses due to the fringing fields. In [2] it is shown that, if designed properly, QD gaps can successfully reduce these losses. Because of these reasons, transformers with distributed or quasi-distributed gaps are now becoming available in commercial markets [3].

**Core loss**

Core loss can be found empirically from the Steinmetz Equation - $kf^{\alpha}B^{\beta}$. It scales rapidly with the frequency of operation and also strongly depends on the magnetic flux density (B) – $\beta$ is usually between 2 and 3. For a given material, reduced volume leads to a higher magnetic field density and hence larger loss. Magnetic components thus need to be kept large when operating at higher frequencies to have tolerable core loss. This is despite them requiring to store less energy per cycle. These trends have led to magnetics increasingly becoming the bottle neck in scaling down the power converter volume. Steinmetz parameters $(k, \alpha, \beta)$ are material dependent and hence the choice of the core material becomes crucial for designing low loss magnetics.

Performance factor ($\mathcal{F} = \hat{B}.f$) is commonly used to compare the performance of materials over a range of frequencies. $\hat{B}$ is the peak AC flux density that leads to a particular power loss density, and $f$ is the operating frequency. While comparing two materials, the material with a higher $\mathcal{F}$, for a particular frequency, can achieve the same

power loss density as the one with a lower $\mathcal{F}$, in a smaller core [10]. This is because higher $\hat{B}$ can be achieved in the core made up of a material with higher $\mathcal{F}$. Likewise, for a given core structure, a material with higher performance factor will have lower losses for a given operating frequency. In [10] authors have shown that with the available magnetic materials, magnetics can continue to reduce in volume up to tens of MHz if they are not constrained by proximity losses.

**Leakage inductance**

Leakage inductance is a consequence of the flux generated by one winding not linking completely with the other winding. Leakage inductance can become a significant percentage of the magnetizing inductance, especially when the required magnetizing inductance is small. Energy stored in the leakage inductance can significantly deteriorate the efficiency of the converter if it is not recovered in each switching cycle. For example, the flyback converter first stores energy in the magnetizing inductance of the transformer and then later in the switching cycle transfers it to the output. In a practical design some fraction of this energy, equal to the leakage to magnetizing inductance ratio of the transformer, gets stored in the leakage inductance. This stored energy adds to the power loss of the converter if no additional circuitry for recovering the same is included. In which case, the percentage loss in the efficiency is equal to the leakage to magnetizing inductance percentage. Thus, a leakage to magnetizing inductance ratio of 2-3% would lead to a 2-3% drop in the efficiency. Such a large drop in efficiency due to one source alone would be unacceptable in most designs. The energy in the leakage inductance resonates with the $C_{oss}$ of the switch in the circuit resulting in a possibly large $V_{DS}$ across the switch which would then have to be rated for a larger voltage.

Some power converter architectures incorporate leakage inductance in the main power stage – for example in an LLC resonant converter. While incorporating this parasitic leakage inductance in the power stage is straightforward in some converters, in others (like in a flyback converter or a coupled inductor based boost converter), clamping circuits need to be added. This increases the hardware complexity and circuit cost. Figure 1 shows that for commercially available Flyback-transformers, as the magnetizing inductance reduces to values below $1\mu H$, leakage inductance can become more than 10% of the magnetizing inductance which might be unacceptable for many power converters.

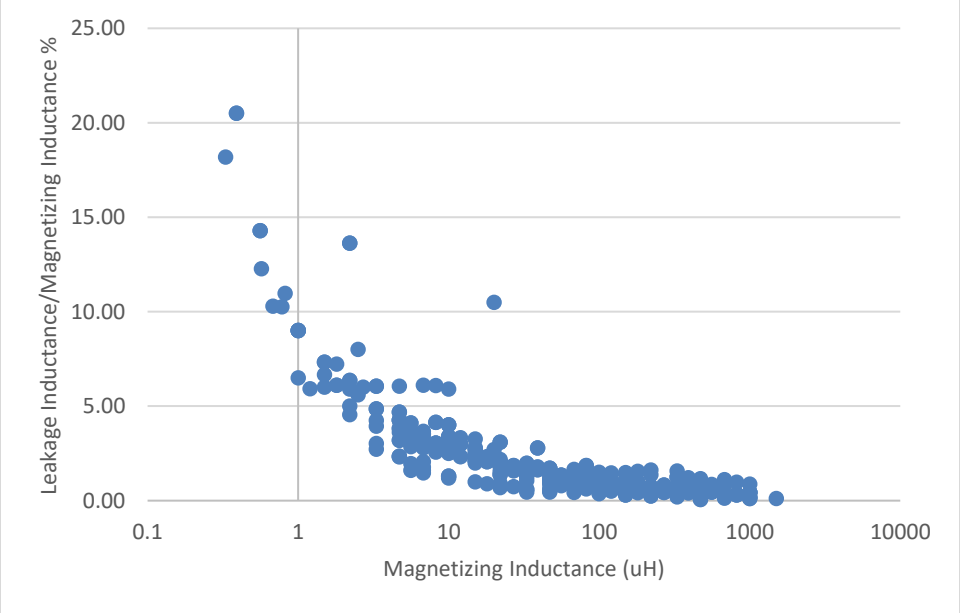


Figure 1 Leakage and Magnetizing inductances of commercially available energy storage transformers

One common way of reducing the leakage inductance is by packing the conductors as tightly as possible. However, it can lead to additional power losses due to the mutual resistance of the windings. This is especially true when the primary and

secondary currents are not in-phase with each other [4]. For converters like Flyback, the losses due to mutual resistance could be quite large.

Using foil windings instead of circular windings can help in reducing the leakage inductance. It is possible to pack the foil windings tightly to achieve better coupling. Foils being wide also provide larger reluctance to the flux flowing across the window. If designed carefully, a transformer with foil windings can leverage the larger surface area of the foils to also reduce the losses due to skin effect. These advantages have been exploited before to achieve designs with low leakage as in [5] and [6]. However, to maximize these benefits, the foils need to be wide and should be packed with little spacing between the adjacent turns. This can lead to a design with large parasitic capacitances which could be a concern for high frequency applications [18].

The above challenges, in the form of high frequency losses and leakage inductances, and limitations of the available solutions call for exploring new strategies for designing magnetics for application in high frequency power converters.

We show that utilizing appropriately sized Quasi-Distributed (QD) gaps to achieve balanced H-fields on either side of the winding helps in achieving low leakage inductance and low conduction losses. As stated previously, QD gaps have been shown to reduce the winding losses due to fringing fields [2]. In [7], QD gaps were used to design an inductor with balanced H-fields on the two sides of the winding. This helped in achieving current conduction across the entire skin of the conductor (double sided conduction), thus mitigating the proximity effect losses. Because of this, the inductor had lower HF AC resistance. The proposed transformer achieves low loss as in [7] and also has a low leakage inductance making it suitable for use in a high frequency power converter requiring an energy storage transformer or a coupled inductor.

## ACHIEVING LOW LEAKAGE INDUCTANCE AND LOW LOSS IN AN HF TRANSFORMER WITH QUASI-DISTRIBUTED GAPS

In this work, we examine a transformer structure which is suitable for high frequency (HF) applications. The proposed transformer structure utilizes quasi-distributed (QD) gaps that are sized such that the H-fields in the airgaps in the center-post and outer-shell are equal, like in [7]. This results in near zero MMF drop across the core window which leads to the transformer achieving low leakage inductance. In addition to low leakage, the transformer also provides significant benefits in the form of reduced AC resistance. Because of the balanced H-fields on the two sides of the conductors, the current flows along most parts of the skin of the conductor [7]. Another benefit of using the proposed structure is the ease with which one can parallel the turns of the primary or the secondary windings. In a structure with a lumped gap, it becomes difficult to ensure equal current sharing between the paralleled turns because the turns close to the gap, and hence near the high H-field region, carry most of the current leading to poor utilization of the winding. In the proposed structure however, the paralleled turns share the current almost uniformly because each turn is in a similar magnetic environment as every other turn. These features (better utilization of the conductor and near-equal current sharing between the paralleled turns of the winding) lead to lower conduction losses as compared to conventional structures without requiring the use of litz wire. Balancing of H-fields in the airgaps of the center-post and outer-shell of the transformer structure also leads to even distribution of the B-fields in the core. This results in better utilization of the core and lower core losses. These excellent properties make this structure suitable for applications in converters operating at multi-MHz frequencies.

We use Finite Element Analysis (FEA) simulations to determine the performance of the transformer and to identify the trade-offs between different parameters like the

wire diameter, window width, aspect ratio of the transformer etc. While operating at multi-megahertz frequencies, the choice of the core material becomes crucial to keep the core losses at an acceptable level. Thus, the selection of the core material is also discussed. The recommended guidelines for designing the proposed HF transformer yield a roughly optimized design. This avoids iterative simulations of multiple transformer structures in FEA software resulting in a significant reduction in the design time.

An example design of a transformer is shown to demonstrate the advantages that the proposed transformer structure provides. A transformer was designed for application in a coupled-inductor based boost converter and the design and prototype construction steps are discussed.

### OVERVIEW OF THE CONTENTS

Chapter 2 details the proposed low loss, low leakage transformer structure. The chapter also provides analysis of the magnetic circuit of the transformer and the various advantages of the same. Chapter 3 discusses the tradeoffs and design guidelines to obtain an optimized transformer. In Chapter 4, the design guidelines presented in Chapter 3 are used to build a 1:10 transformer for a coupled-inductor based boost converter. The chapter provides details about prototype construction and a proposed testing plan of the same. Chapter 5 summarizes the work and provides concluding remarks.

# Chapter 2: A Low-Leakage, Low-Loss Transformer Structure for HF Applications

In this chapter we propose a transformer structure suitable for high-frequency applications. The transformer uses quasi-distributed (QD) gaps on the inner (center-post) and outer cores (outer-shell). The QD gaps are sized such that they achieve equal H-fields on both sides of the winding. The reluctance model of the structure reveals that QD gaps when sized appropriately can achieve zero MMF drop across the window. This leads to a design with low leakage inductance. The balanced H-fields on the two sides of the winding also lead to double sided conduction [7] and hence, reduction in ac losses due to proximity effects. The structure allows paralleling of turns in a transformer with non-unity turns ratio while achieving near uniform distribution of current among the paralleled turns. These two features enable the use of solid wires instead of litz wires while still achieving low conduction losses. The balanced H-fields in the air gaps lead to a more uniform distribution of B-fields in the core and hence lower core loss. In this chapter we explore the conditions when a transformer with the proposed structure achieves low leakage inductance and the parameters that affect leakage the most. Later, we discuss the advantages and tradeoffs associated with the proposed transformer structure.

## GEOMETRY OVERVIEW

The axisymmetric view of the proposed geometry of a 3-turn transformer is shown in Figure 2. The complete model can be obtained by rotating the axisymmetric view along the z-axis. It is similar to a pot core structure with air gaps in the center-post and the outer-shell of the structure. Instead of a single air gap however, the proposed structure has multiple smaller gaps that form a QD gap. Because of the QD gaps, the core

can be a high permeability material while achieving reduced fringing field losses. The number of gaps is the same as the number of turns in the transformer. The gap reluctances are designed to have equal H-fields in the air gaps on the center-post as well as the outer-shell. The center post and outer-shell are made up of thin magnetically permeable discs which are stacked on top of each other. The airgap spacing can be produced by pieces of shim stock. The primary and secondary windings of the transformer are interleaved, and each turn of the primary winding is paired with a secondary turn and each such pair is placed in one core section. The winding is placed in the center of the window. The spacing between the windings and the center-post is an important design decision because it involves a tradeoff between the core and copper losses. These and other design tradeoffs are discussed as part of the design guidelines in the next chapter.

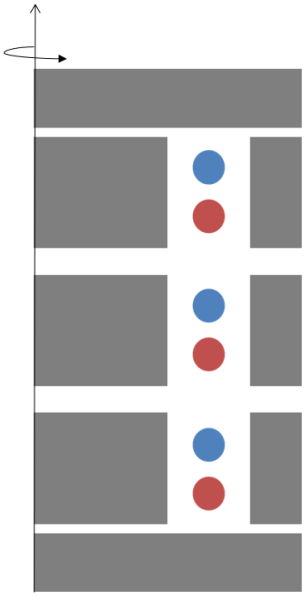

Figure 2 Cross-sectional view of the proposed transformer. Revolving around the z-axis produces the complete pot core structure. Red and blue circles represent the individual turns of the primary and secondary winding respectively.

## RELUCTANCE MODEL AND ANALYSIS FOR LOW LEAKAGE INDUCTANCE

It is shown in this section that the proposed geometry results in the MMF drop across the window reluctance becoming zero. This would mean no flux flows across the window leading to zero leakage inductance. Other parasitic leakage paths, however, allow the flux to flow across the window leading to a non-zero, but small, leakage inductance. It is instructive to note the dependencies of the leakage inductance on various parameters of the structure. We study this next.

To analyze the performance of the proposed structure, we can model the transformer using its magnetic circuit equivalent. The H-field on either side of the winding is designed to be equal. The gap length on the center-post and outer-shell is also designed to be the same. The MMF drop across the two air gap reluctances will thus be the same ($MMF = Hl_g$). Figure 3 highlights the reluctances in different magnetic paths in the proposed structure. Assuming that all the flux flows through the core, the air gap reluctances on either side of the winding should be the same (say $R_g$). The air gaps at the end caps may or may not be designed to have the same reluctance as the air gaps in the middle portion of the structure. We thus name them $R_x$. The MMF contribution of the primary winding (or the combined MMF contribution due to the current in the primary and secondary winding) is represented by an MMF source $V_p$ (see Figure 4). Some flux lines will take a path across the window to complete their loop – starting from an airgap on one side of the winding to the one directly on the other side. Let this flux that flows across the window experience a reluctance of $R_w$. The resultant reluctance model is shown in Figure 4.

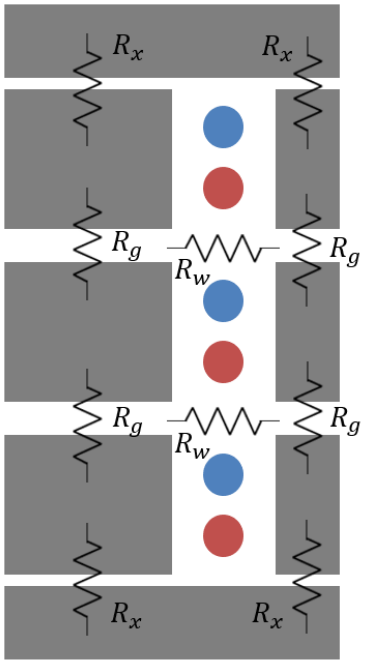


Figure 3 Cross-sectional view of the proposed transformer structure showing air gap reluctances ($R_g$ and $R_x$) and window reluctance ($R_w$).

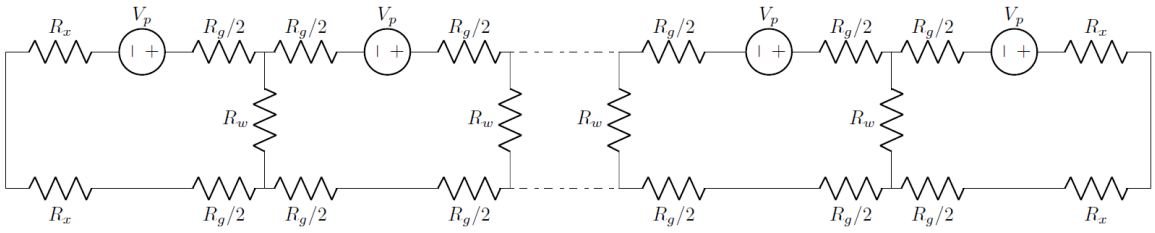


Figure 4 Magnetic circuit model of a n-gap transformer structure, like the one shown in Figure 3. $R_g$ and $R_x$ are airgap reluctances. $R_w$ models the reluctance of the flux path across the window.

For an n-stage network, the MMF drop across the $i^{th}$ $R_w$ can be given by the sum of the MMF contributions by the sources on the right of the $i^{th}$ $R_w$ ($V_{\{R_{w_i}\}_{right}}$) and those on its left ($V_{\{R_{w_i}\}_{left}}$).

$$V_{\{R_{w_i}\}_{left}} = \frac{\big((i-1)(2R_g)+R_z\big)}{2R_z+(n-2)(2R_g)}(n-i)V_p \quad (1)$$

$$V_{\{R_{w_i}\}_{right}} = \frac{\big((n-2)-(i-1)\big)(2R_g)+R_z\big)}{2R_z+(n-2)(2R_g)}(i)(-V_p) \quad (2)$$

Here, $R_z$ is equal to $2R_x + R_g$. By setting $V_{\{R_{w_i}\}_{right}} = V_{\{R_{w_i}\}_{left}}$, we find that the MMF drop across $R_{w_i}$ becomes zero when $R_x = 0.5 \times R_g$. Thus, if the length of air gap at the endcaps is half of the length of air gap in the center post, we get zero flux through the window reluctances. Any flux that flows across the window will not link with all the turns of the other winding and hence will contribute to leakage. Thus, making flux through all $R_w s$ equal to zero should yield zero leakage inductance for a simple reluctance model as in Figure 4.

In the above discussion, however, we did not model a parasitic leakage path which corresponds to the reluctance $R_a$ shown in Figure 5. As flux through $R_w s$ is nearly eliminated because of the balanced QD gaps, the fluxes flowing through these parasitic paths start to dominate and become the major contributors to leakage inductance. Figure 7 shows the flux through the two $R_w s$ and three $R_a s$, found analytically, in the magnetic circuit equivalent of the structure (Figure 6). At $R_x = 0.5 \times R_g$, the fluxes through $R_w s$ become equal and are very small in magnitude (but not zero because of the presence of $R_a s$ in the magnetic circuit). The fluxes through $R_a s$ are the dominant contributors to the flux through the reluctance paths in the window. In Figure 7, while analyzing the circuit, the total reluctance in the core (due to $R_g$ and $R_x$) is kept constant and the reluctances in the window paths ($R_a s$ and $R_w s$) are assumed to be fifty times $R_g$ when $R_g$ is one (in reality, the window path reluctances would be much higher than $50 \times R_g$).

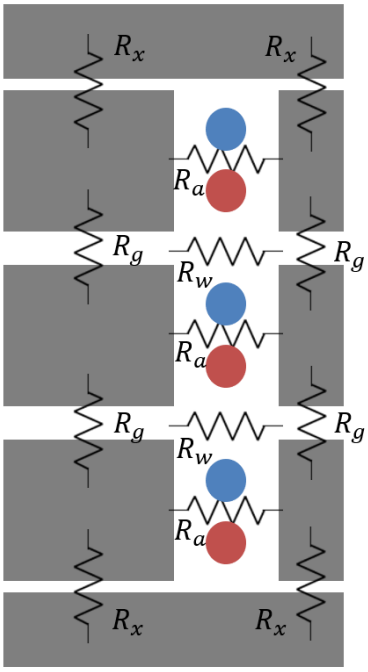


Figure 5 Cross-sectional view of the proposed transformer showing the various reluctances in the magnetic flux paths including the parasitic path, $R_a$.

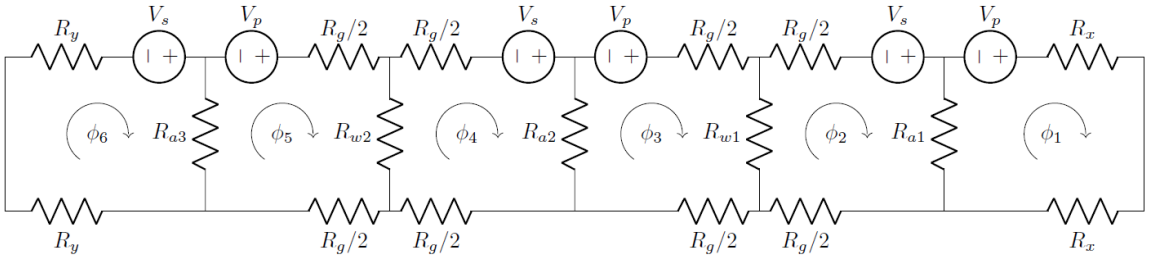


Figure 6 Magnetic circuit model of the structure shown in Figure 5.

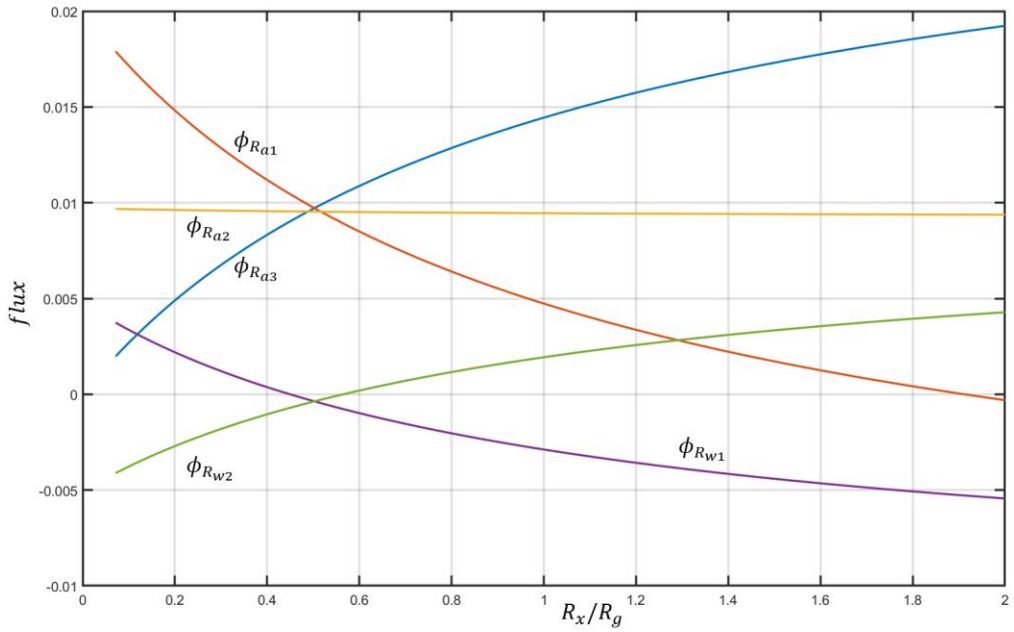


Figure 7 Flux flowing through the various paths in the window i.e., through $R_w s$ and $R_a s$ when primary was excited and secondary was open. Window path reluctances were kept constant ($R_w s = R_a s = 50$). Total reluctance in the core ($4R_g + 4R_x$) was also kept constant.

## LEAKAGE INDUCTANCE

The magnetic circuit of Figure 6 can be used to find an expression for the leakage inductance in terms of the flux flowing through the reluctances in the window paths. Analysis of reluctance model of the magnetic circuit as presented below is similar in concept to the "Physical Modelling" of the magnetic structure [19]. Because we are modeling each turn of a winding separately, it allows us to model even the flux that is linking with only some turns of the same winding. For simplicity, we are ignoring any fringing paths. Here, $V_s$ is the MMF corresponding to the current in the secondary turns and $V_p$ is the MMF due to the primary turns. $\phi_1$ through $\phi_6$ are fluxes in the six circuit loops. $\phi_{ra1}$ through $\phi_{ra3}$ are the fluxes flowing in the reluctances denoted as $R_a$ in Figure 6. Similarly, $\phi_{rw1}$ and $\phi_{rw2}$ are fluxes through the two $R_w$s. To find the self and

mutual inductances of the primary and secondary windings, first, the primary winding is excited with a current of 1A with secondary open. The flux flowing through the $V_p$ MMF sources correspond to the total flux that is linking with the primary winding ($\lambda_{11}$) and flux flowing through $V_s$ MMF sources corresponds to the total flux linking with the secondary winding ($\lambda_{12}$).

$$L_{11} = \frac{\lambda_{11}}{I_1} = \phi_1 + \phi_3 + \phi_5 \tag{3}$$

$$L_{12} = \frac{\lambda_{12}}{I_1} = \phi_2 + \phi_4 + \phi_6 \tag{4}$$

$\phi_1$ through $\phi_6$ can be written in terms of $\phi_{ra_i}$ and $\phi_{rw_i}$ as below

$$\phi_6 = m\phi_{ra3} \tag{5}$$

$$\phi_5 = (1+m)\phi_{ra3} \tag{6}$$

$$\phi_4 = (1+m)\phi_{ra3} + \phi_{rw2} \tag{7}$$

$$\phi_3 = (1+m)\phi_{ra3} + \phi_{ra2} + \phi_{rw2} \tag{8}$$

$$\phi_2 = (1+m)\phi_{ra3} + \phi_{ra2} + \phi_{rw2} + \phi_{rw1} \tag{9}$$

$$\phi_1 = (1+m)\phi_{ra3} + \phi_{ra2} + \phi_{ra1} + \phi_{rw2} + \phi_{rw1} \tag{10}$$

Here, $m$ is equal to $\frac{2R_y}{R_a}$

The leakage inductance on the primary is thus given by,

$$L_{lkg_p} = L_{11} - L_{12} = \sum \phi_{ra_i} \tag{11}$$

A similar procedure can be followed to find $L_{22}, L_{21}\ and\ L_{lkg_s}$.

$$L_{lkg_s} = L_{22} - L_{21} = -\sum \phi_{ra_i} \tag{12}$$

Note that the values of $\phi_{ra_i}$ would be different in the two states, when the primary is excited and when the secondary is excited if the structure is not symmetrical – for example, when the reluctances on the bottom and top disks ($R_x$ and $R_y$ ) are not equal.

In the presence of the flux paths corresponding to $R_a$, leakage inductance in the proposed structure is determined by the flux flowing through the path between the coils of the same pair and not by the flux flowing through $R_w s$. We, thus, need to minimize the flux flowing through these paths to reduce the leakage inductance. This can be achieved by making the reluctance Ra as large as possible.

A MATLAB script was written to perform circuit analysis of the magnetic circuit of Figure 6. Figure 8 shows the variation in the leakage inductance as calculated using the above method when $R_x$ and $R_y$ are changed. The reluctances of flux paths through the window, i.e., $R_a s$ and $R_w s$ were kept constant. While plotting the graphs, the total reluctance in the outer loop, the one corresponding to the flux path through the core, was kept constant. That is, the sum, $2R_x + 2R_y + 4R_g$ was kept constant. This is because while designing for a target magnetizing inductance and a known number of turns (usually chosen considering the tradeoffs between core and copper losses), the reluctance introduced in the core is the control variable available to the designer.

It can be seen from the 3D-plot of Figure 8 that a symmetric structure i.e., $R_x = R_y$ is desirable. Figure 8 also shows that $L_{lkg}$ decreases as $2(R_x + R_y)/R_g$ increases. This means that if we are designing a transformer considering only the leakage inductance as the design parameter then a symmetric structure with lumped gaps at the endcaps will achieve a lower leakage inductance than the proposed structure. However, rarely are the transformers designed considering only the leakage inductance. Even though a QD-gapped structure with $R_x = R_y = 0.5R_g$ does not correspond to the minimum leakage inductance, the proposed structure has relatively low leakage. In addition to this, it has some important advantages compared to a structure with symmetrical lumped gaps at the endcaps ($R_g = 0$ and $R_x = R_y$). These include low effective resistance because of double sided conduction and the ability to parallel turns of

the transformer while achieving equal current sharing. These have been discussed in the next section. Figure 9 shows the dependence of $L_{lkg}$ on the window reluctance. It can be seen that because of close to zero MMF drop across $R_w$, leakage inductance has little sensitivity towards the value of $R_w$ especially when it is greater than a few tens of $R_g$. This is typically the case in most designs.

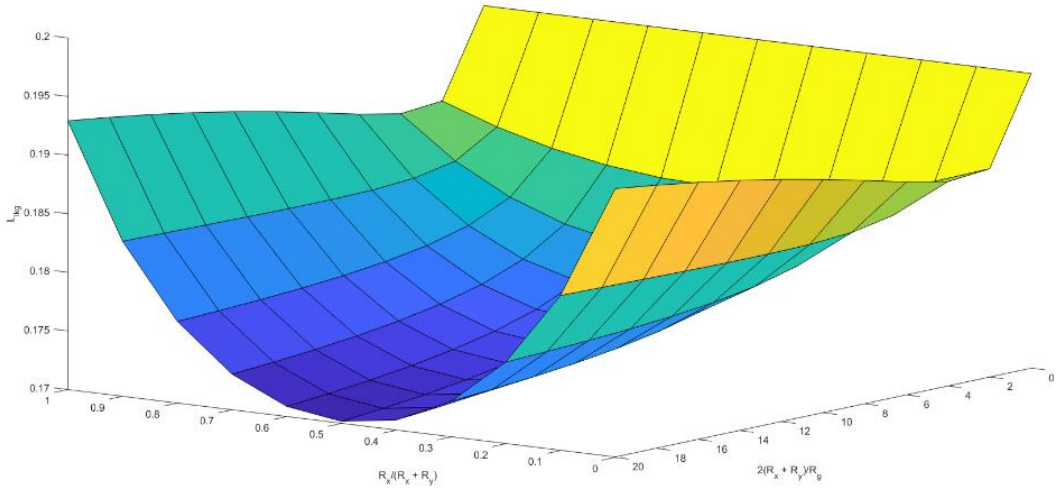


Figure 8 Leakage inductance calculated according to the method shown in this section as a function of $R_x/(R_x + R_y)$ (a proxy for how symmetric the gaps at endcaps are) and $2(R_x + R_y)/R_g$ (a proxy for how distributed the QD gaps are). The reluctances are normalized to $R_g$.

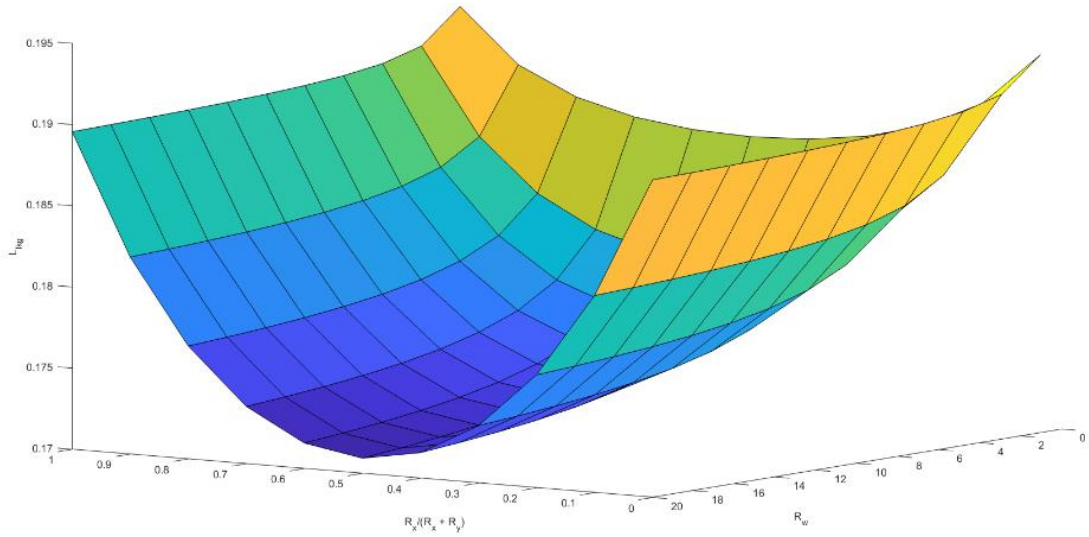


Figure 9 Leakage inductance calculated according to the method shown in this section as a function of $R_x/(R_x + R_y)$ and $R_w$. The reluctances are normalized to $R_g$.

## ADVANTAGES OF THE PROPOSED STRUCTURE

### Current distribution in the conductors – Double sided conduction

Because the MMF drop across $R_{w_i}$ is very close to zero, the H-field in the region corresponding to $R_w$ is close to zero for all turns of the winding. The H-field on the two sides of the winding, i.e., in the air gaps in the outer-shell and the center-post, is designed to be equal. Because of the balanced H-fields on the two sides of the winding, the current does not crowd towards a particular region in the conductor but spreads out relatively evenly along the skin of the conductor. This is similar to double-sided conduction achieved in [7]. It is important to note that double sided conduction is achieved even when the currents in the two windings are out of phase i.e., when only one winding carries current at a time. Unlike a conventional interleaved transformer, which will

experience large losses due to the induced eddy currents in the conductors, the proposed structure achieves low loss even when the primary and secondary windings are in quadrature with each other.

Figure 10 shows current distribution in the conductors of a transformer with the proposed structure. The almost uniform current distribution leads to lower HF AC conduction losses. The current maintains ‘double sided conduction’ in all the turns on the transformer. This is because each pair of the primary and secondary turns is in a magnetically similar environment in a QD-gapped structure. This is in contrast to a lumped gap structure in which the turns closest to the gap are in a region with large H-fields and the other conductors are in regions with very little H-field. Because the current crowds near the surface closest to larger H-fields, in a lumped gap structure, the turns closest to the gap will experience larger current crowding and higher resistance. The QD-gapped structure achieves double sided conduction in each turn of the winding, because of which the proposed structure will have lower AC resistance and will potentially be the preferred choice in most applications. Impedance matrices of two transformers, one with the proposed structure and other with a lumped gap are shown in Table 1. The proposed structure achieves significantly lower resistance matrix values. When carrying 5A current in the primary with the secondary open, the solid loss in the proposed structure was 1.44W and that in the structure with a lumped gap was 44.1W.

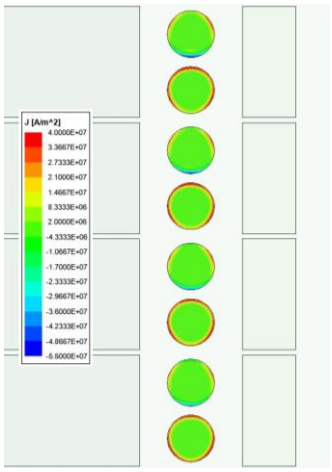


Figure 10 Current distribution seen in FEA simulation of a structure with balanced QD gaps on the center post and outer shell of the pot core structure. Transformer achieves almost uniform current distribution along the skin of the conductor

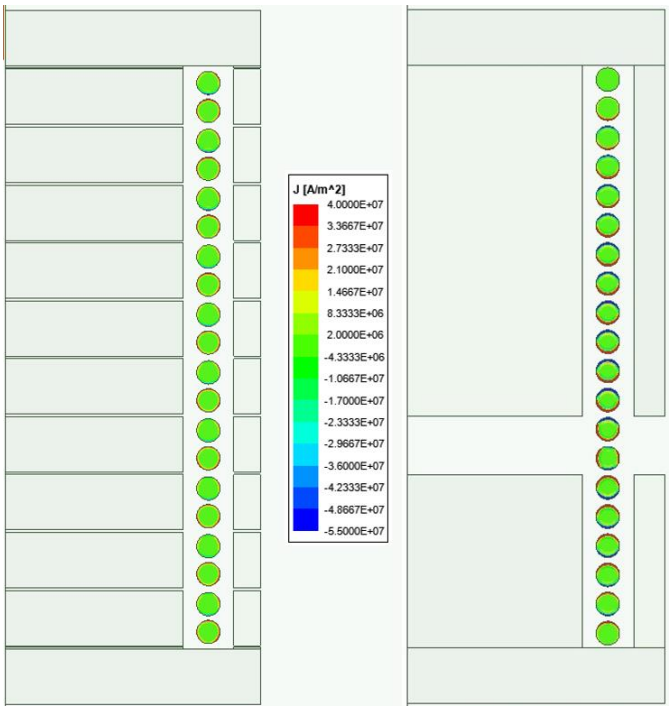


Figure 11 FEA simulations of 10-10 transformers – one with the proposed structure (left) and other with a lumped gap. Impedance matrices of the two structures obtained from ANSYS Maxwell simulations are shown in Table 1

Table 1 Impedance matrix comparison of the structures shown in Figure 11. Apart from the air gaps, the two transformers were otherwise similar.

| Proposed structure | | | |
|---|---|---|---|
| $R_{11}, L_{11}$ | $0.115(\Omega)$, $10.21(\mu H)$ | $R_{12}, L_{12}$ | $-0.003(\Omega)$, $10.13(\mu H)$ |
| $R_{21}, L_{21}$ | $-0.003(\Omega)$, $10.13(\mu H)$ | $R_{22}, L_{22}$ | $0.115(\Omega)$, $10.21(\mu H)$ |
| Structure with a single lumped gap | | | |
| $R_{11}, L_{11}$ | $3.53(\Omega)$, $10(\mu H)$ | $R_{12}, L_{12}$ | $3.71(\Omega)$, $10.17(\mu H)$ |
| $R_{21}, L_{21}$ | $3.71(\Omega)$, $10.17(\mu H)$ | $R_{22}, L_{22}$ | $4.16(\Omega)$, $10.55(\mu H)$ |

**"1 to N" transformers – Uniform current distribution in paralleled turns**

To achieve a lower leakage inductance in a non-unity turns ratio transformer, one can add parallel turns to the winding with fewer turns to make the number of coils in that winding equal to that of the other winding. The primary and secondary windings can then be interleaved to achieve better coupling between the two windings [18]. In the presence of a lumped gap however, the current distribution in the paralleled turns is far from even. The paralleled turn closest to the high H-field region carries the most current. This results in poor utilization of the conductors and leads to higher conduction losses.

In the QD gapped transformer, the turns can be paralleled while still achieving almost uniform distribution of current in the paralleled turns. This is a consequence of all the conductor pairs being in a magnetically similar environment as described in the previous section. Table 2 and Table 3 show the comparison between the current distribution in the paralleled turns of 1-10 transformers, one with a QD gap and the other with a single lumped gap. It can be seen that the proposed design has much better current sharing than the conventional design. Better current sharing between the paralleled turns will result in lower conduction losses and hence better performance.

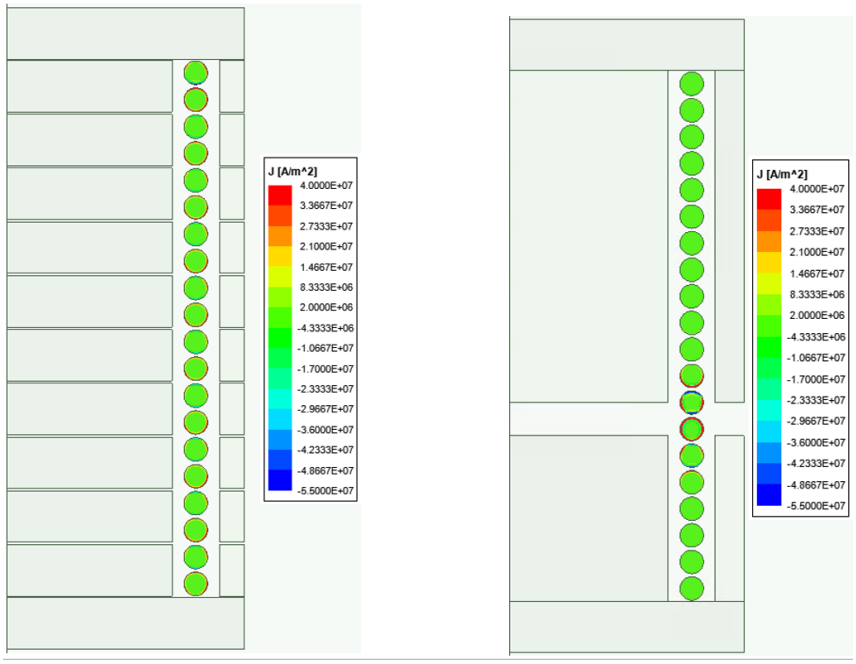


Figure 12 FEA simulations of 1-10 transformer showing the current distribution. Left – proposed structure. Right – structure with interleaved primary and secondary windings and a lumped gap. Both are designed for the same $L_{mag}$ and are carrying the same amount of current.

Table 2 Current distribution seen in FEA simulation in the primary winding of a 1-10 transformer with the proposed structure.

| Turn | Current (A) |
|---|---|
| 1 | 8.202 |
| 2 | 6.14 |
| 3 | 5.896 |
| 4 | 5.745 |
| 5 | 5.667 |
| 6 | 5.652 |
| 7 | 5.698 |
| 8 | 5.813 |
| 9 | 6.025 |
| 10 | 5.162 |

Table 3 Current distribution seen in FEA simulation in the primary winding of a 1-10 transformer with interleaved primary and secondary windings and lumped gaps.

| Turn | Current (A) |
|---|---|
| 1 | 0.408 |
| 2 | 0.18 |
| 3 | 0.17 |
| 4 | 0.164 |
| 5 | 0.3 |
| 6 | 13.075 |
| 7 | 42.325 |
| 8 | 2.875 |
| 9 | 0.2 |
| 10 | 0.3 |

**Sensitivity of $L_{lkg}$ to the window path reluctances**

As discussed previously, in the proposed structure, the MMF drop across the window reluctances is approximately zero. Thus, changing the window reluctance, $R_w$, does not significantly affect the flux flowing across the window and hence, the sensitivity of the leakage inductance to the window reluctance is very low. In the structure with lumped gaps at the endcaps, however, the MMF drop across the $R_w s$ is not close to zero. This leads to the lumped gap structure being more sensitive to the value of $R_w$. For smaller values of $R_w$, the structure with lumped gaps at the endcaps loses its advantage of having lower leakage inductance. Both the structures, however, are quite sensitive to the reluctance of the flux path between the conductors of the same pair, i.e., $R_a$. Reducing $R_a s$ would lead to larger flux flowing through that path leading to larger leakage

inductance. To keep the leakage inductance small, it is important to keep $R_a$ as large as possible.

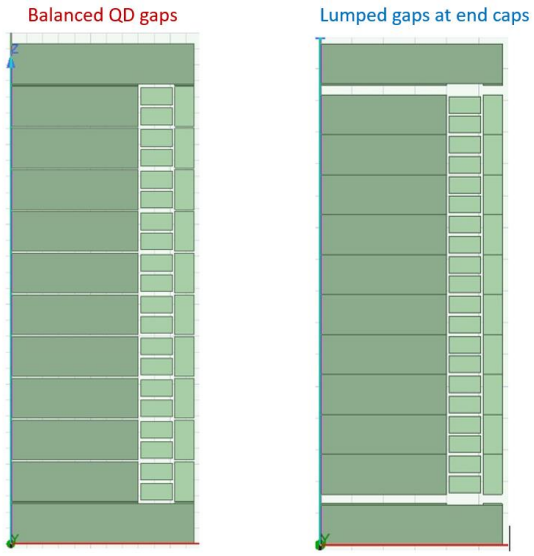


Figure 13 Transformer structures ($L_{mag} = 10\mu H$) with "balanced QD gaps" and "lumped gaps at endcaps" that were simulated in ANSYS Maxwell.

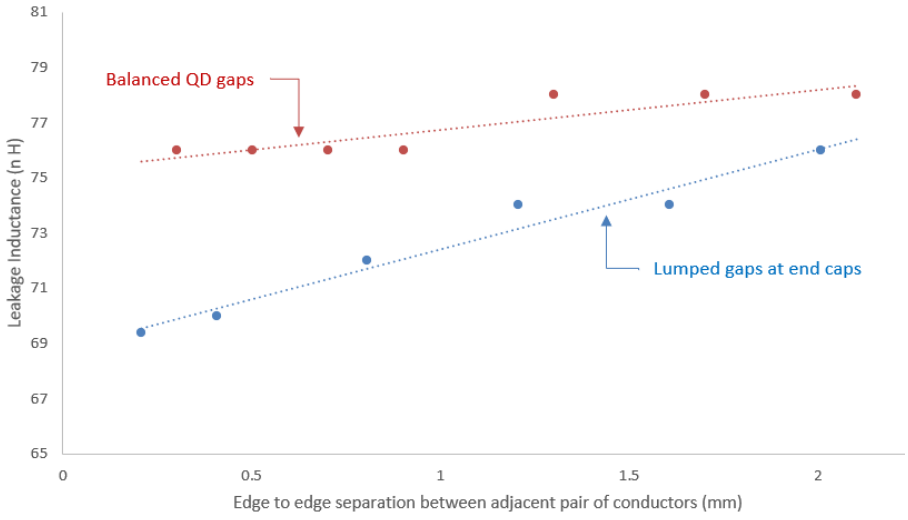


Figure 14 Variation in the leakage inductance with changes in the spacing between pairs ($R_w$) as seen in the FEA simulations.

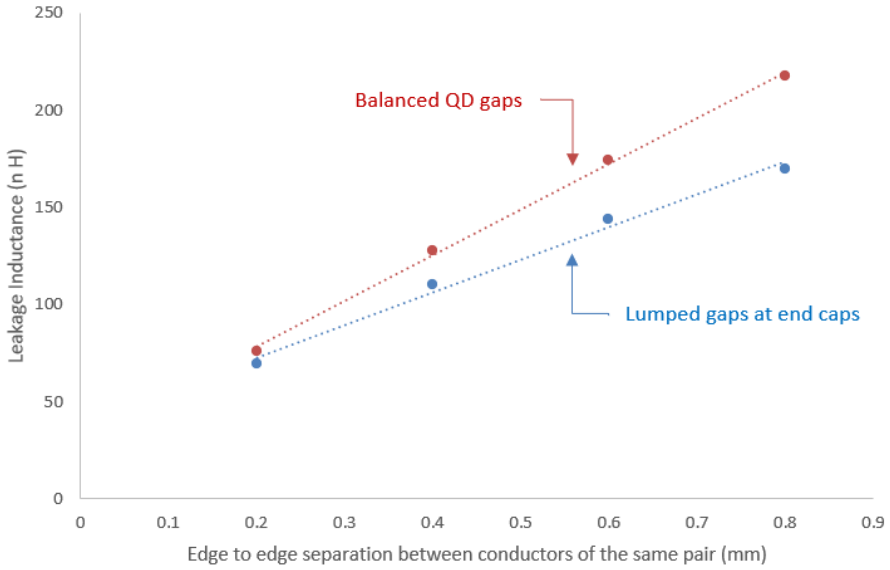


Figure 15 Variation in the leakage inductance with changes in the spacing between primary and secondary conductors of the same pair ($R_a$) as seen in the FEA simulations.

### SENSITIVITY OF LEAKAGE INDUCTANCE TO VERTICAL MISALIGNMENT OF TURNS

Because of the helical nature of the winding, the primary and secondary turns will remain in the exact center of the core-section only at one instance in an entire turn. To quantify the effect of this misalignment on the leakage inductance, a 1-10 turns transformer with a magnetizing inductance of 105nH (the design of which is discussed in Chapter 4) was simulated with windings misaligned from the center of the core section (displaced vertically). As can be seen from Figure 16, the leakage inductance is not sensitive to this misalignment. To accommodate the helical nature of the winding, an extra layer of core pieces needs to be added in the center-post and outer-shell.

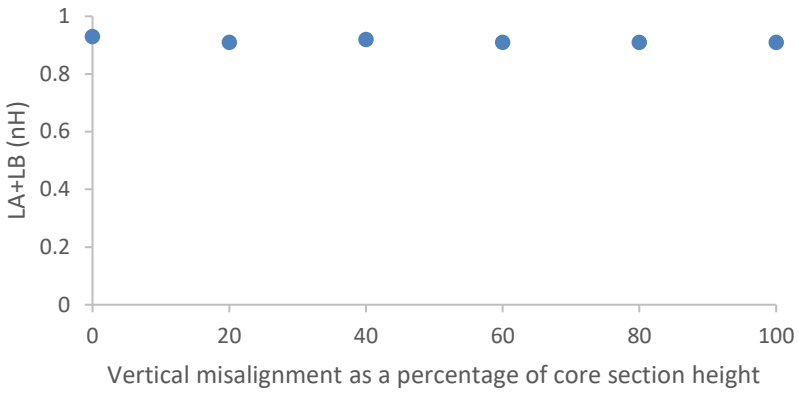


Figure 16 Total leakage inductance (both primary and secondary leakage inductances referred to the 1-turn side) as seen in FEA simulations vs. vertical misalignment of the winding. Leakage inductance is not very sensitive to misalignments.

## RELUCTANCE MODEL IN THE PRESENCE OF FRINGING

As shown previously, the reluctance model can be used to predict the leakage and magnetizing inductances. The reluctance model can be analyzed in a Spice simulator to quickly verify and understand the dependence and sensitivity of the leakage and magnetizing inductances on different reluctances and hence the geometry of the structure. This can help reduce the design time because the much slower FEA simulations can be performed once the design parameters are roughly optimized in the faster Spice simulators. Thus, finding the reluctances of the structure to a satisfactory degree of accuracy can be useful for designers.

Finding the reluctance of a relatively large air gap is non-trivial because of fringing of the magnetic flux near the air gap. Fringing increases the effective cross-sectional area seen by the flux and leads to a reduced reluctance. The reluctance of the air gaps can be found using the method suggested in [8]. The 2-D reluctances proposed in [8] can be extruded in the z-direction (outside the plane of the paper) by appropriately

choosing the equivalent z-extrusion for a pot core structure. For example, the "post-to-post" reluctance $\left(R_{post,post3(b)}\right)$ given in [8] can be extruded by an effective out of plane length of $p_c/2$ (where $p_c$ is the perimeter of the center-post) to get the net reluctance of the airgap in the center-post (described as $R_{g_{c_m}}$ later).

The following formulae for the gap reluctances in the center-post ($R_{g_{c_m}}, R_{g_{c_{ec}}}$) and outer-shell ($R_{g_{o_m}}, R_{g_{o_{ec}}}$) are seen to produce inductance matrices in LTSpice that are sufficiently similar to those obtained from FEA simulations (see Figure 19 to Figure 21). Here, the subscript $ec$ refers to the airgap at the endcaps and subscript $m$ refers to all the other airgaps.

$$R_{g_{c_m}} \approx \frac{1}{\frac{p_c}{2}\mu_0\left(\frac{r_c}{l_g}+\frac{2}{\pi}\left(1+\ln\left(\pi\frac{h_c}{2l_g}\right)\right)\right)} \tag{13}$$

$$R_{g_{c_{ec}}} \approx \frac{1}{\frac{p_c}{2}\mu_0\left(\frac{r_c}{l_{gx}}+\frac{4}{\pi}\left(1+\ln\left(\pi\frac{h_c}{4l_{gx}}\right)\right)\right)} \tag{14}$$

$$R_{g_{o_{m1}}} \approx \frac{1}{p_{o_{in}}\mu_0\left(\frac{t_s}{2l_g}+\frac{1}{\pi}\left(1+\ln\left(\pi\frac{h_c}{2l_g}\right)\right)\right)} \tag{15}$$

$$R_{g_{o_{m2}}} \approx \frac{1}{p_{o_{out}}\mu_0\left(\frac{t_s}{2l_g}+\frac{1}{\pi}\left(1+\ln\left(\pi\frac{h_c}{2l_g}\right)\right)\right)} \tag{16}$$

$$R_{g_{o_m}} \approx \frac{R_{g_{o_{m1}}} \times R_{g_{o_{m2}}}}{R_{g_{o_{m1}}}+R_{g_{o_{m2}}}} \tag{17}$$

$$R_{g_{o_{ec1}}} \approx \frac{1}{p_{o_{in}}\mu_0\left(\frac{r_c}{2l_{gx}}+\frac{2}{\pi}\left(1+\ln\left(\pi\frac{h_c}{4l_{gx}}\right)\right)\right)} \tag{18}$$

$$R_{g_{o_{ec2}}} \approx \frac{1}{p_{o_{out}}\mu_0\left(\frac{r_c}{2l_{gx}}+\frac{1}{\pi}\left(1+\ln\left(\pi\frac{h_c}{2l_{gx}}\right)\right)\right)} \tag{19}$$

$$R_{g_{o_{ec}}} \approx \frac{R_{g_{o_{ec1}}} \times R_{g_{o_{ec2}}}}{R_{g_{o_{ec1}}}+R_{g_{o_{ec2}}}} \tag{20}$$

Here, $l_g$ and $l_{gx}$ are the air gap lengths in the middle portion of the center-post and at the endcaps respectively. $r_c$ is the radius of the center post, $h_c$ is the height of each core section, $p_c$ is the perimeter of the center-post, $t_s$ is the thickness of the outer shell, $p_{o_{in}}$ and $p_{o_{out}}$ are the inner and outer perimeters of the outer-shell. Similar reluctance models have been used in the literature before for different transformer structures to successfully find reluctance in the presence of fringing [8], [9].

Equations for airgap reluctances presented till now include fringing between two adjacent sections of the core which reduces the reluctance of the airgap. The overall fringing path outside the structure is shown in Figure 17. Incorporating a separate fringing reluctance, $R_f$, to model the net fringing path of the flux outside the structure [7] increased the agreement between the values obtained from Spice and FEA simulations. The resultant reluctance model is shown in Figure 18.

$$R_f \approx \frac{0.9}{\mu_0 \pi r_t} \tag{21}$$

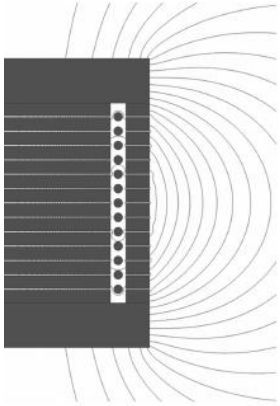

Figure 17 Fringing field of a structure with quasi-distributed gaps. The fringing field is similar to that of an air core solenoid. Image taken from [7].

The window reluctances are harder to model when circular conductors are used. To validate the reluctance model, we consider a design with rectangular conductors. These can either be PCB tracks in a planar transformer or square conductors. The window reluctances can be calculated by the below formulae. $p_s$ and $c_s$ are the edge-to-edge spacings between conductors of the adjacent pairs and of same pair, respectively.

$$R_w = \frac{1}{\mu_0 \times 2\pi p_s} \ln\left((r_t - t_s)/r_c\right) \tag{22}$$

$$R_a = \frac{1}{\mu_0 \times 2\pi c_s} \ln\left((r_t - t_s)/r_c\right) \tag{23}$$

Using the above reluctance modeling, simulations were performed in ANSYS Maxwell for a 1-1 transformer with 10 series connected turns. The values of the inductance matrices obtained from the FEA simulations and the reluctance model are shown in Figure 19 – Figure 21. The spacing between adjacent conductors was kept the same in all structures (i.e., $R_a s$ and $R_w s$ were kept constant). The leakage inductances calculated from the reluctance model agree with those obtained from FEA simulations and both follow a similar trend. The structure with two lumped gaps at the end caps achieves a lower leakage inductance than the structure with balanced QD gaps ($R_x = R_y = R_g/2$). This is as per the trend seen in Figure 8. Despite the lower leakage inductance, the structure in Figure 20 will not be preferred for most applications because of the higher resistance due to current crowding on the turns closest to the endcaps as seen in Figure 22. The structure in Figure 19 has low leakage as well as low resistance because of conduction along most parts of the skin of the conductor and little current crowding as explained previously in this chapter.

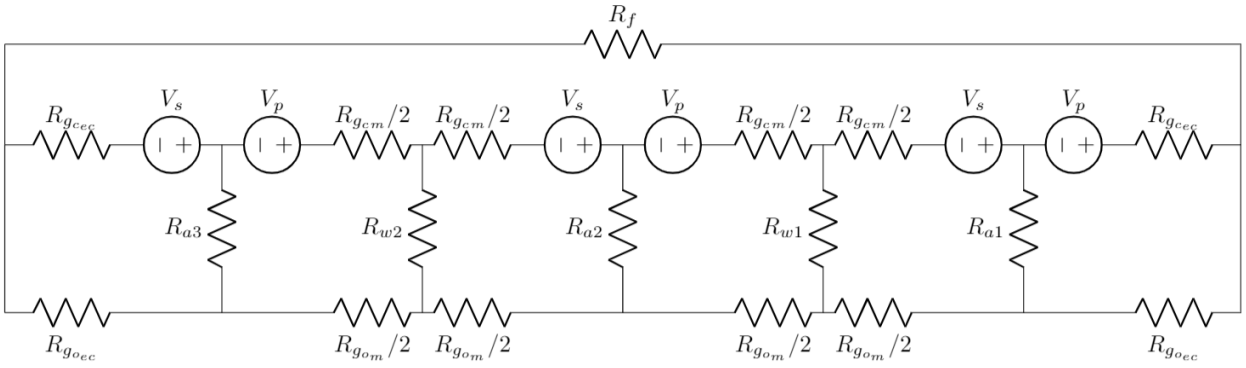


Figure 18 Magnetic circuit model of the structure shown in Figure 5 considering the local (bulging of magnetic fields in the gaps) and overall (as shown in Figure 17) fringing paths.

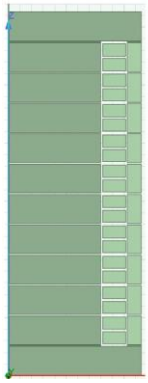

Figure 19 Transformer with proposed QD-gapped structure ($l_g = 0.11mm$ and $l_x = 0.055mm$). Expected inductance matrix values according to reluctance model and ANSYS Maxwell are shown in the below table.

Table 4 Inductance matrix values for structure in Figure 19 found using ANSYS Maxwell and reluctance model.

| Inductance Matrix obtained using: | $L_{11}$ | $L_{12} = L_{21}$ | $L_{22}$ | $L_{lkg}$ |
|---|---|---|---|---|
| ANSYS Maxwell | $10.052\mu H$ | $10.014\mu H$ | $10.052\mu H$ | $76nH$ |
| Reluctance model without fringing | $6.6791\mu H$ | $6.699\mu H$ | $6.6791\mu H$ | $58.44nH$ |
| Proposed reluctance model | $9.9062\mu H$ | $9.8767\mu H$ | $9.9062\mu H$ | $59nH$ |

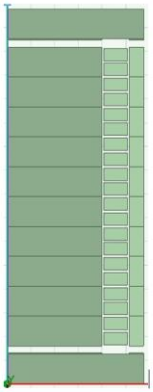

Figure 20 Transformer with lumped gaps at end caps ($l_g = 0.015mm$ and $l_x = 0.625mm$). Expected inductance matrix values according to reluctance model and ANSYS Maxwell are shown in the below table.

Table 5 Inductance matrix values for structure in Figure 20 found using ANSYS Maxwell and reluctance model.

| Inductance Matrix obtained using: | $L_{11}$ | $L_{12} = L_{21}$ | $L_{22}$ | $L_{lkg}$ |
|---|---|---|---|---|
| ANSYS Maxwell | $10.175\mu H$ | $10.14\mu H$ | $10.175\mu H$ | $70nH$ |
| Reluctance model without fringing | $6.1416\mu H$ | $6.1155\mu H$ | $6.1416\mu H$ | $52.086nH$ |
| Proposed reluctance model | $11.071\mu H$ | $11.043\mu H$ | $11.071\mu H$ | $55.3nH$ |

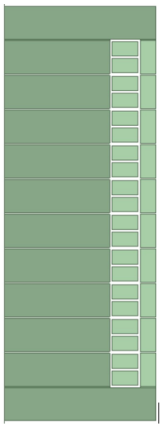

Figure 21 Transformer with unbalanced QD gaps ($l_g = 0.125mm$ and $l_x = 0mm$). Expected inductance matrix values according to reluctance model and ANSYS Maxwell are shown in the below table.

Table 6 Inductance matrix values for structure in Figure 21 found using ANSYS Maxwell and reluctance model.

| Inductance Matrix obtained using: | $L_{11}$ | $L_{12} = L_{21}$ | $L_{22}$ | $L_{lkg}$ |
|---|---|---|---|---|
| ANSYS Maxwell | $10.154\mu H$ | $10.115\mu H$ | $10.154\mu H$ | $78nH$ |
| Reluctance model without fringing | $6.5253\mu H$ | $6.4523\mu H$ | $6.5253\mu H$ | $145.91nH$ |
| Proposed reluctance model | $9.856\mu H$ | $9.8272\mu H$ | $9.856\mu H$ | $59.3nH$ |

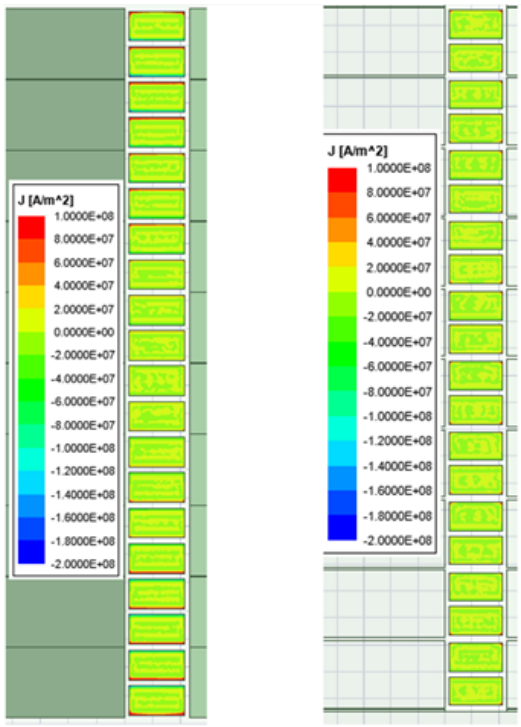


Figure 22 Current distribution in the turns of transformers of Figure 19 and Figure 20.

In this chapter we analyzed a transformer structure with QD gaps and found that with $R_x = 0.5R_g$ and balanced H-fields on the two sides of the winding, the structure achieves low high frequency conduction losses because of current conduction along most of the skin of the conductor. The QD gap allows paralleling of turns of a winding while achieving near equal current sharing among the paralleled turns. With the balanced QD gaps, we can achieve near zero MMF across the window which leads to a design with low leakage inductance. These properties make the proposed structure suitable for applications in power converters operating at multi-MHz frequencies with high currents and requiring high conversion ratios.

# Chapter 3: Design Guidelines for Optimized Design

The design guidelines provided in this chapter aim to reduce the power loss of the proposed transformer by choosing the optimum design parameters. To find the trade-offs, an HF transformer with QD gaps was designed in ANSYS Maxwell for a given magnetizing inductance and volume. The effect of various design choices on the winding resistance, leakage inductance and the core and copper losses of the transformer was observed and optimum values of the design parameters in terms of mathematically defined quantities have been proposed. Because of the shallow optimums observed in the simulations, minor variations from the optimized parameters, because of manufacturing tolerances for example, should not affect the performance of the structure noticeably.

### SIMULATION SETUP

To test the various trade-offs in the choice of different parameters like the window width, wire diameter, end cap thickness and the aspect ratio, simulations were performed in ANSYS Maxwell. The goal of the simulations was to find the optimum design of a transformer with balanced quasi-distributed gaps for use in a coupled-inductor boost converter. The details of the power converter are presented in the next section. The simulated transformers had a magnetizing inductance of 105nH and a turns ratio of 1-10. Ten turns of the primary winding were paralleled and interleaved with the secondary turns. The volume of the transformer was constrained to $r_t = 0.5\ [in], h_t = 1\ [in]$. Because of the ability to achieve double sided conduction, solid wires can be used while keeping the copper losses reasonably low. Eliminating the requirement of litz wire to keep the copper losses low is one of the advantages of the proposed design. Material-80 from Fair-Rite Products Corp. was used as the core material for all the simulations. Appendix A describes the procedure used for finding the core and copper losses in

ANSYS Maxwell. A transient simulation with the primary and secondary currents, as shown in Figure 23, was setup to calculate the average copper and core losses. The 2-D axisymmetric structure of the transformer is shown in Figure 24 with relevant parameters marked.

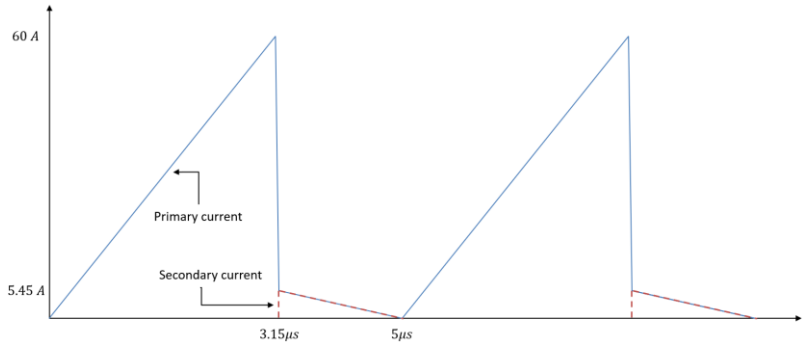


Figure 23 Current excitations in primary and secondary windings of the simulated transformer

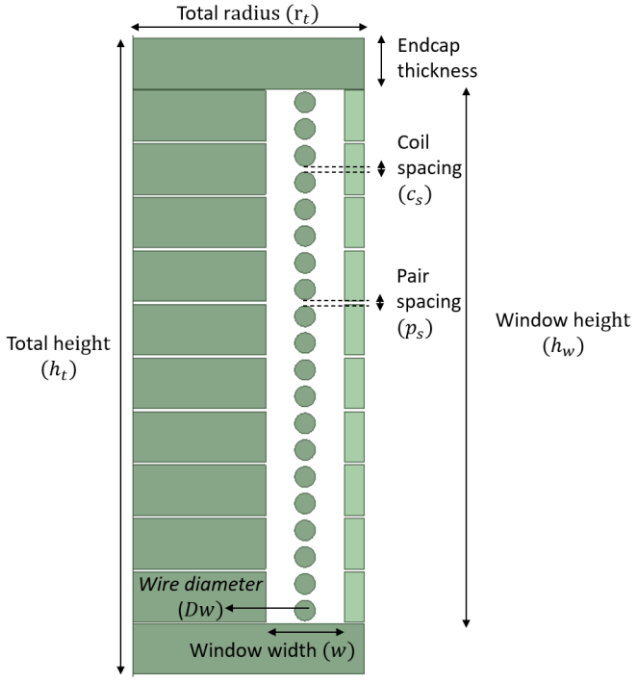


Figure 24 Radial cross-section of the proposed transformer structure. Design parameters defining the geometry are marked.

### BALANCE THE H-FIELDS ON EITHER SIDE OF THE WINDING

If the H-field on one side of the winding is more than the other side, the current in the conductor crowds near the edge closest to the high H-field region. This current crowding leads to larger conduction losses. By balancing the H-field on the two sides of the conductor, one can achieve double sided conduction [7]. This leads to lower copper losses at high frequencies as compared to a conventional transformer with lumped gap as discussed in Chapter 2. To achieve equal H-fields on the two sides of the winding, a method similar to [7] was used. Balancing the MMF drops across the gaps on the center-post and the outer-shell will lead to equal H-fields because the effective lengths are same ($MMF = Hl_g$). This is achieved by making the total reluctance on the center-post equal to the total reluctance in the outer-shell. Figure 21 shows the lumped reluctance model of the structure. Here, $R_{c_{post}}$ is the reluctance of the core in the center-post. $R_{g_{post}}$ is the reluctance of the air gap in the center-post. Similarly, $R_{c_{shell}}$ and $R_{g_{shell}}$ are the reluctances of the core and the air gap of the outer-shell. By sizing the center-post and the outer-shell to balance the reluctances, as per the below equation, we can achieve equal H-fields on the two sides of the wire. The dimensions can be further tweaked in the FEA software to achieve better balanced H-fields.

$$R_{c_{post}} + R_{g_{post}} = \left(R_{c_{shell}} + R_{g_{shell}}\right) || R_f \tag{24}$$

$R_f$ is the overall fringing reluctance given by Equation 21. It is found by modeling the fringing fields of the proposed structure as the fringing fields from an air core solenoid. It is shown in [7] that $R_f$ accurately models the fringing path reluctance of a structure with QD gaps.

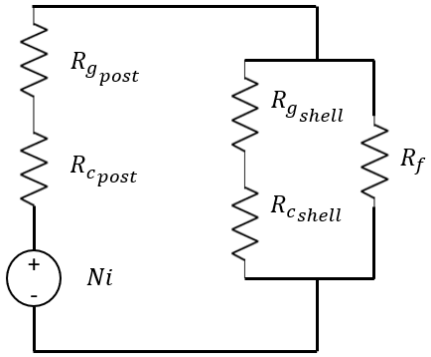


Figure 25 Magnetic circuit model of a QD gapped structure with lumped reluctances of the air gaps and core pieces. [7]

### UNIFORM DISTRIBUTION OF B-FIELDS IN THE CORE

To reduce core loss, the B-field should be distributed uniformly in all the regions of the core. Because the core losses scale as $B^{\beta}$ (with $\beta$ usually between 2 and 3), core sections with larger B-fields will experience substantially higher core loss and deteriorate the performance of the transformer.

With the proposed design, it is possible to achieve uniform distribution of the B-field in the core by choosing core materials with the same permeability for the center-post and outer-shell. Since $B = \mu H$, balancing the H-fields in the center-post and outer-shell lead to the same B-fields in the two regions if $\mu$ is the same for both. Thus, the proposed sizing of the center-post and outer-shell for this structure will yield lower core loss if the center-post and outer-shell are made from the same material or materials with similar permeability.

### CHOICE OF WIRE DIAMETER – VERTICAL FILL

For a given window height, the choice of the wire diameter determines the spacing between the adjacent conductors. Even in a skin depth limited case, a larger wire diameter will provide larger conduction area leading to lower copper losses. However, as

the wire diameter increases, losses due to proximity effect between the turns of the transformer increase. We can define a metric, Vertical Fill ($F_v$), to quantify the wire size required to minimize the conduction losses. Vertical Fill is defined as,

$$F_v = \frac{2ND_w}{h_w} \tag{25}$$

Here, N is the number of turns of the primary or secondary winding – whichever is greatest, $h_w$ is the height of the window and $D_w$ is the diameter of the wire.

As the wire diameter is increased, either the edge to edge spacing between two coils of the same pair ($c_s$) can be reduced or the edge to edge spacing between two pairs ($p_s$) can be reduced. It can be seen from Figure 26 and Figure 27 that increasing the wire diameter while reducing the distance between the conductors helps in reducing the conduction losses initially. Beyond ~90% vertical fill, the proximity losses start to dominate. While performing these simulations, the width of the window was kept three times the diameter of the biggest wire that would fit (wire corresponding to $F_v = 100\%$) so that the effects due to fringing field with changing wire diameter are negligible [7]. A vertical fill between 85 and 95% gives low conduction losses in this transformer.

In a transformer with paralleled turns, like the one being simulated in this chapter, the QD gaps lead to an almost but not exactly equal current division between the turns. Even though small, the difference between the current division leads to some H-field in the region between the pairs (in the region right next to the airgaps). It is because of the proximity losses due to this H-field that conduction losses increase for higher $F_v$ in Figure 26. Figure 28 and Figure 29 show the results of similar simulations performed for a 10-10 transformer (with the same geometrical structure) with peak primary current of 6A instead of 60A. The shapes and frequency of the current waveforms were otherwise similar to that shown in Figure 23. It can be seen that in this case the conduction losses

do not increase at higher $F_v$ when $p_s$ is being decreased. This is because of the near zero H-field in that region. As expected, decreasing $c_s$ leads to increased losses. Thus, for a unity turns ratio transformer, it is recommended to have very low spacing between conductors of adjacent pairs while spacing apart the conductors of the same pair to achieve a $F_v$ of 75-90%.

For a given window width, the spacing between the conductors decides the reluctance of the flux paths across the window. The smaller is the spacing, larger are the window path reluctances ($R_a$ and $R_w$). As seen from Figure 14, to keep the leakage inductance small, $R_a$ should be made as large as possible. Increasing the conductor diameter beyond the minimum in Figure 27 helps in reducing the leakage inductance at the cost of increased conduction losses. For a leakage constrained design, $F_v$ greater than 90% should be used.

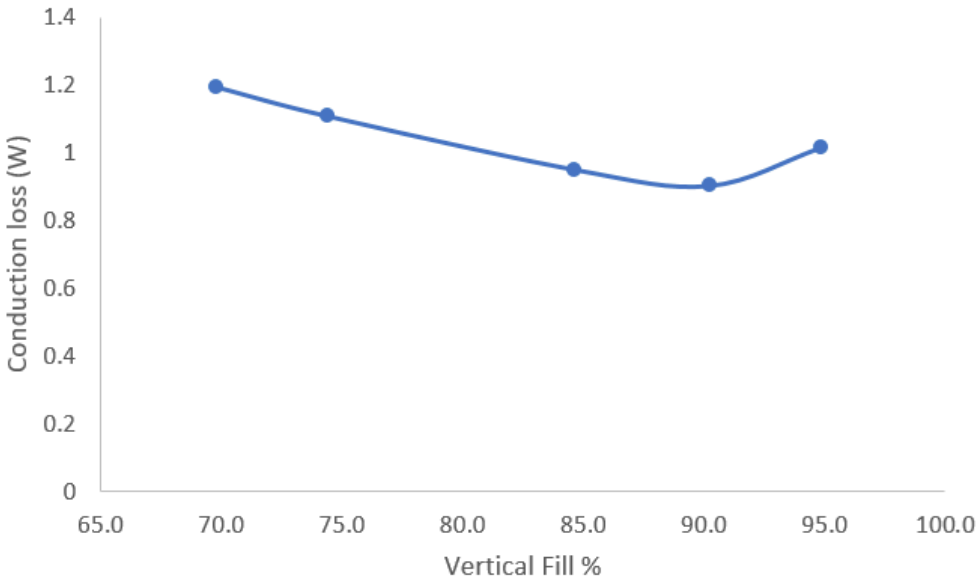


Figure 26 Conduction losses plotted against vertical fill when the spacing between conductor pairs ($p_s$) is reduced while keeping spacing between conductors of same pair ($c_s$) constant. The simulated transformer had a turns ratio of 1-10 and an approximately 1:1 aspect ratio ($r_t = 12.7mm, h_t = 26.6mm$)

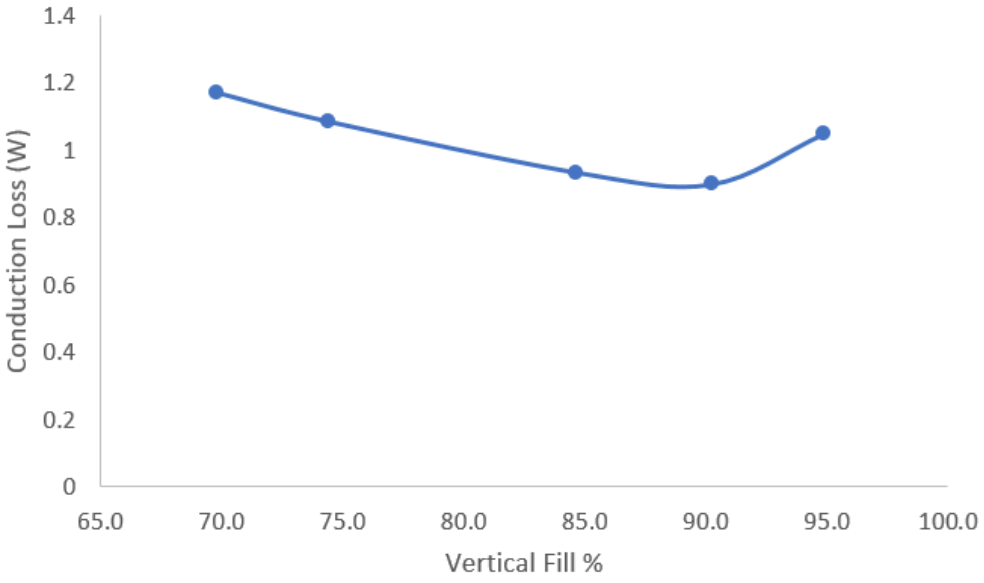


Figure 27 Conduction losses plotted against vertical fill when the spacing between conductors of the same pair ($c_s$) is reduced while keeping spacing between two pairs ($p_s$) constant. The simulated transformer had a turns ratio of 1-10 and an approximately 1:1 aspect ratio ($r_t = 12.7mm, h_t = 26.6mm$)

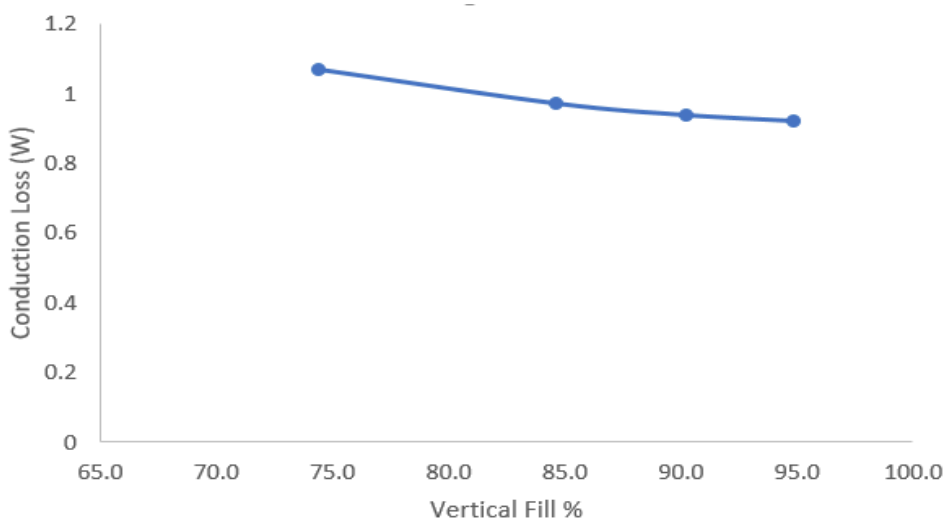


Figure 28 Conduction losses plotted against vertical fill when the spacing between conductor pairs ($p_s$) is reduced while keeping spacing between conductors of same pair ($c_s$) constant. The simulated transformer had a turns ratio of 10-10 and an approximately 1:1 aspect ratio ($r_t = 12.7mm, h_t = 26.6mm$)

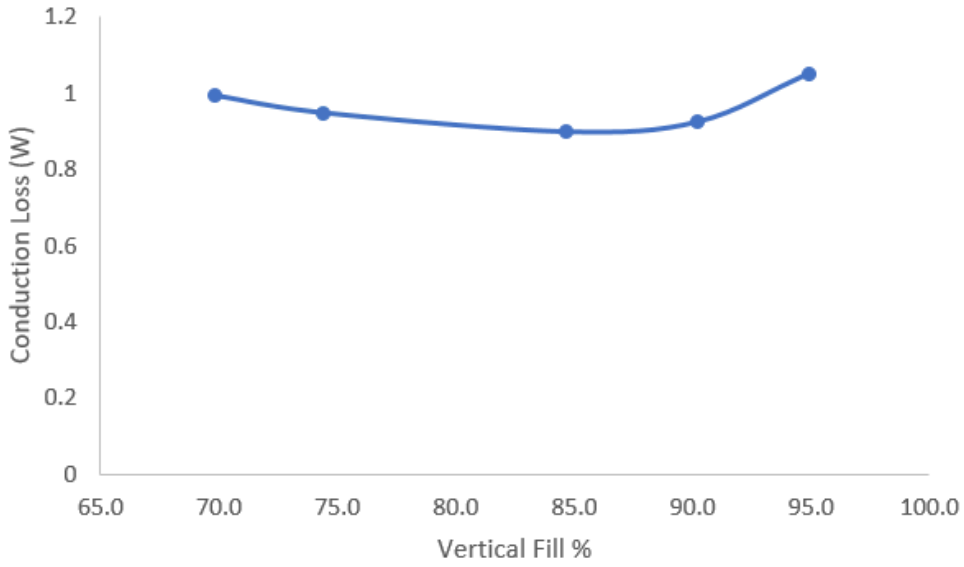


Figure 29 Conduction losses plotted against vertical fill when the spacing between conductors of the same pair ($c_s$) is reduced while keeping spacing between two pairs ($p_s$) constant. The simulated transformer had a turns ratio of 10-10 and an approximately 1:1 aspect ratio ($r_t = 12.7mm, h_t = 26.6mm$)

### CHOICE OF WINDOW WIDTH – HORIZONTAL FILL

Once the wire diameter has been chosen to keep the conduction losses and leakage inductance low, the window width should be chosen such that the total losses in the transformer are minimized. To reduce the conduction losses due to fringing fields, the windings should be placed far away from the gaps. This would require having a wide window. For a known volume, a desired $L_{mag}$ and given current excitation, wider window would mean narrower center-post and thus, larger B-fields. Hence, wider windows would lead to increased core losses. Flux crowding near the window corners will also contribute to core losses. Wider window means the volume of these high B-field regions would increase leading to worse core loss. Thus, the choice of the window width involves a tradeoff between core and conduction losses for a given volume. We can define a metric, Horizontal Fill ($F_h$), to quantify the optimum window width ($w$).

$$F_h = \frac{D_w}{w} \tag{26}$$

Figure 30 shows the core and copper losses for different Horizontal Fills. Figure 31 shows total loss for different transformer structures with the same magnetizing inductance but different $F_h$ and $F_v$ values. Because of larger conduction losses for $F_v = 96\%$, as explained in the previous sub-section, the performance of that structure is inferior to the one with $F_v = 80\%$. It can be seen that the optima are shallow and maintaining a horizontal fill between 40-60% keeps the total losses low. As detailed in [2], the gap pitch (p) and the spacing between the conductors and the gaps (s) should satisfy the condition $p < 4 \times s$ for keeping the losses due to fringing fields low. Appendix B shows that many combinations of $F_v$ and $F_h$ in the recommended ranges agree with the recommendations of [2]. Larger values of $F_h$ lead to a larger leakage inductance because of reduced window reluctances ($R_a s$ and $R_w s$). Thus, designing at the lower end of the $F_h$ range is better for a leakage constrained design.

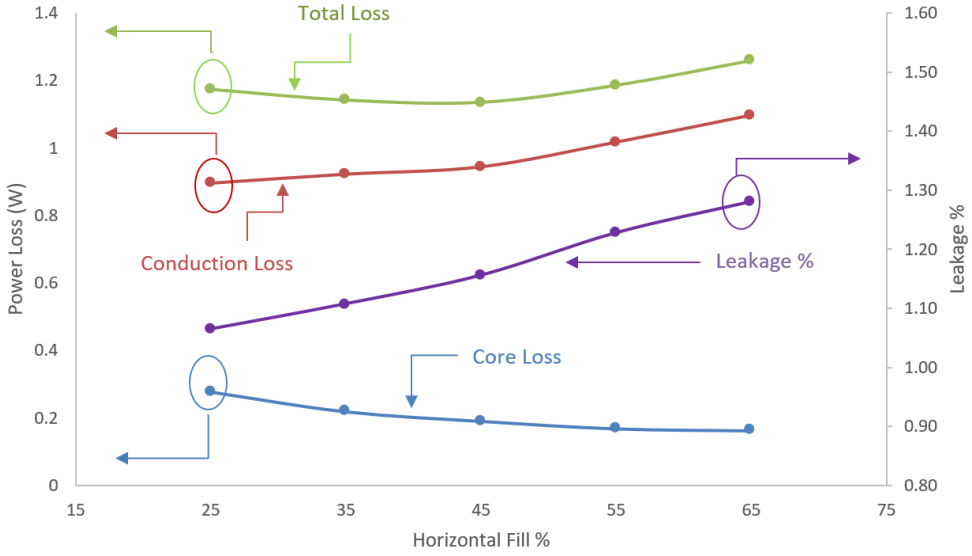


Figure 30 Power losses observed in FEA simulations for different $F_h$. Leakage inductances on the primary and that on the secondary referred to primary were used to find leakage as percentage of magnetizing inductance. The transformer had a square aspect ratio (height ≈ diameter). $F_v$ = 85%.

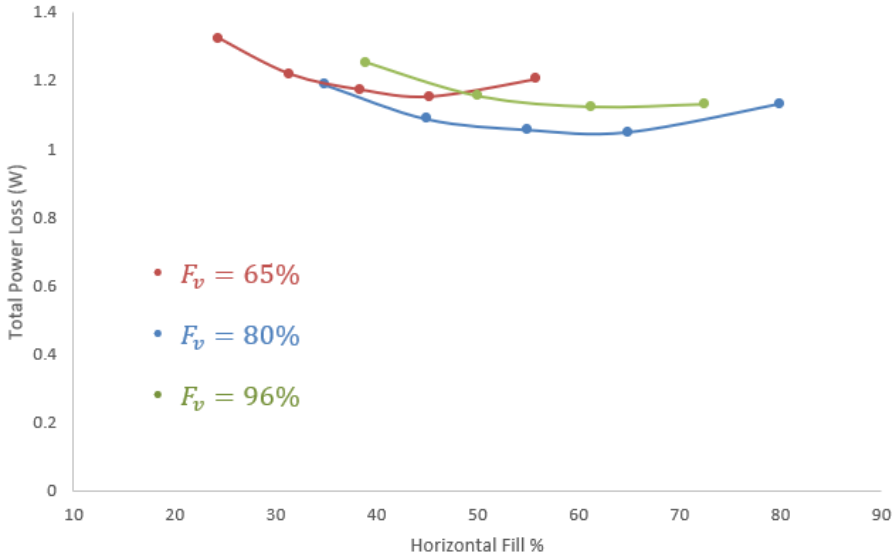


Figure 31 Total power loss observed in FEA simulations for different $F_h$ and $F_v$. The transformer had a 3:2 aspect ratio (height ≈1.5× diameter).

### APPROXIMATELY BALANCE THE CORE AND COPPER LOSSES – ASPECT RATIO

For a given volume, the transformer can either have a square aspect ratio (height ≈ diameter) or it can be tall and skinny or short and wide. In magnetics constrained by AC losses instead of saturation of the core or low frequency losses, the total loss is usually minimized when core and copper losses are approximately balanced [7]. Balanced core and copper losses can also be thought of as better utilization of the core material and the copper in the structure. To achieve this, usually, the number of turns and air gap length are changed. However, in a high turns-ratio transformer, achieving a balance between the core and conduction losses using this strategy is not easy because even a small increase in the number of turns requires a substantial decrease in the wire diameter to make it fit in the same volume.

Instead of changing the number of turns, one can change the aspect ratio of the transformer. While sacrificing on core loss, a taller structure would allow the use of wires

with larger diameters for the same $F_v$ resulting in lower copper losses. Choice of 3:2 aspect ratio (height ≈ 1.5 ×diameter) for the transformer under consideration leads to a more balanced core and copper loss distribution (see Figure 32).

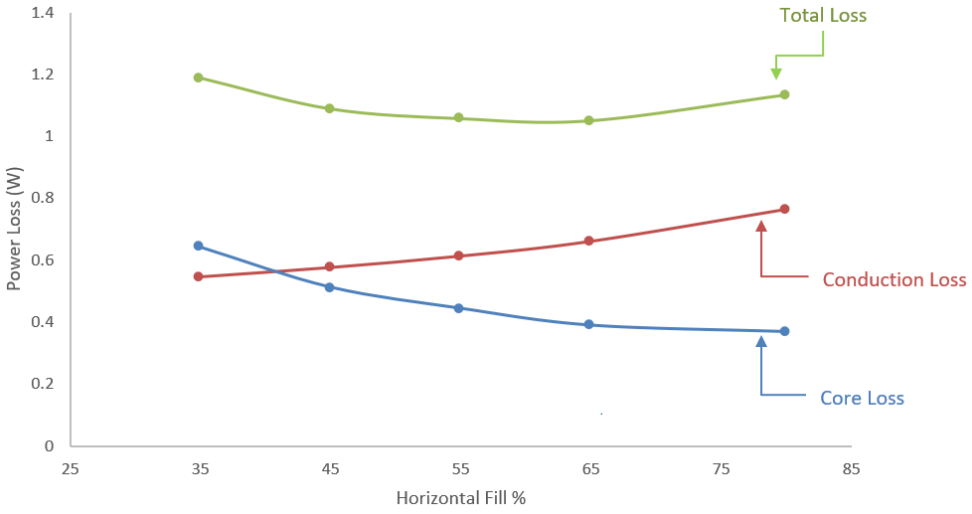


Figure 32 Losses observed in FEA simulations of the transformer for different $F_h$. The transformer had a 3:2 aspect ratio (height ≈1.5× diameter). $F_v$ =85%.

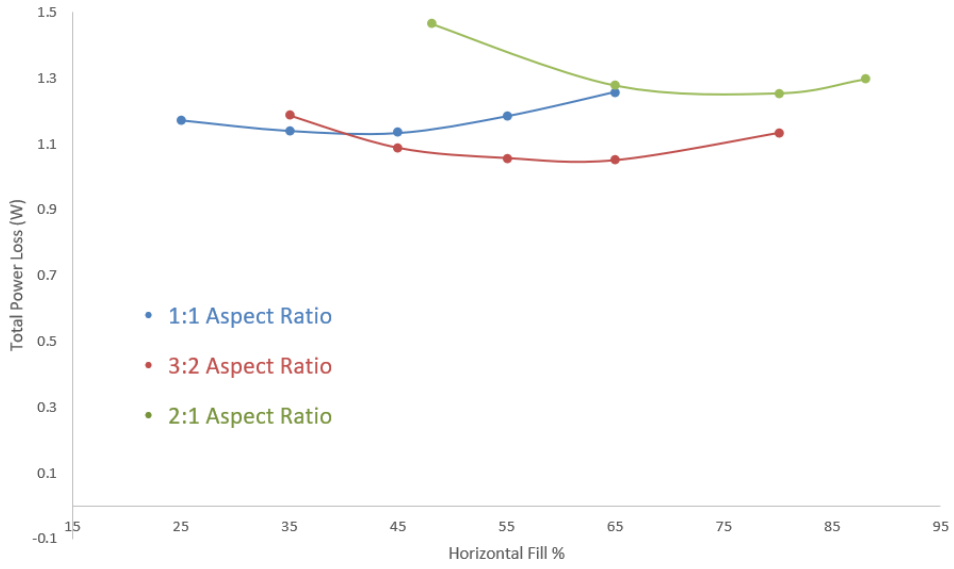


Figure 33 Total power loss observed in FEA simulations for different Aspect Ratios. All structures had a vertical fill of ≈ 85%.

### END CAPS

The end caps have high B-field regions where the flux crowds near the edges of the window. Making the end caps taller would allow the B-fields to spread out more, leading to lower core losses. This, however, leads to increased volume and has diminishing returns (Figure 35). It is recommended to tune the height of the endcaps after the choice of the center-post radius, outer-shell thickness and wire diameter has been made. FEA simulations can be run to achieve as uniform distribution of B-fields as possible while considering its tradeoff with volume.

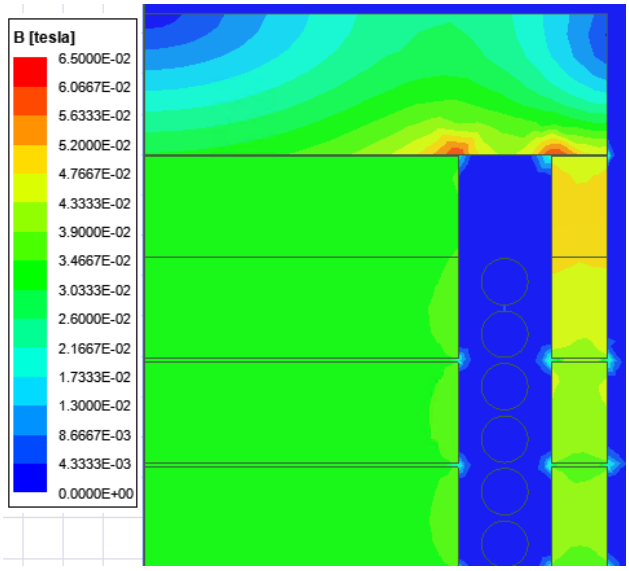


Figure 34 Larger B-fields (red) in the end caps at the edges of the window.

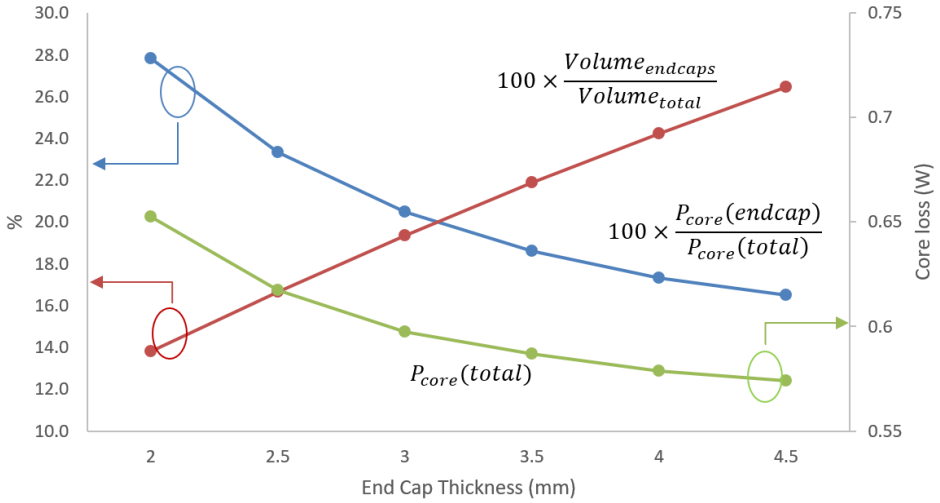


Figure 35 Thicker endcaps lead to lower power losses. This, however, is at a cost of increased volume.

## CORE MATERIAL

The choice of core material is an important design decision especially for multi-MHz operation. Performance factor ($\mathcal{F}$) is commonly used to compare the performance of materials over a range of frequencies.

$$\mathcal{F} = \hat{B}.f \tag{27}$$

Here, $\hat{B}$ is the peak of the AC flux density that results in a particular power loss density and $f$ is the frequency of operation. While comparing two materials, the material with a higher $\mathcal{F}$, for a particular frequency, can achieve the same power loss density as the one with a lower $\mathcal{F}$, in a smaller core [10]. This is because higher $\hat{B}$ can be achieved in the core made up of a material with higher $\mathcal{F}$. Likewise, for a given core structure, a material with higher performance factor will have lower losses for a given operating frequency. Thus, comparing performance factors of different core materials for the operating frequency is a quick way of identifying the best suited core material for the application.

In [10], authors have plotted the Performance Factors for different core materials in the MHz frequency range. It can be seen that, amongst the materials tested, Material-67 from Fair-Rite Products Corp. had the highest performance factor for the frequencies of interest, 1-5MHz. [11] shows the comparison of Material-67's Performance Factor with the recently launched Material-80. Material-80 has better performance than Material-67 in the frequency range of 1-4MHz. Because today a lot of the high frequency power converters operate in this range, we considered Material-80 for our simulations. Comparing the power loss density graphs of Material-80 and material 3F46 (from Ferroxcube) [16], it can be seen that the performance of the two is similar at the frequencies of interest. Thus, one can also use 3F46 instead of Material-80 and achieve similar performance.

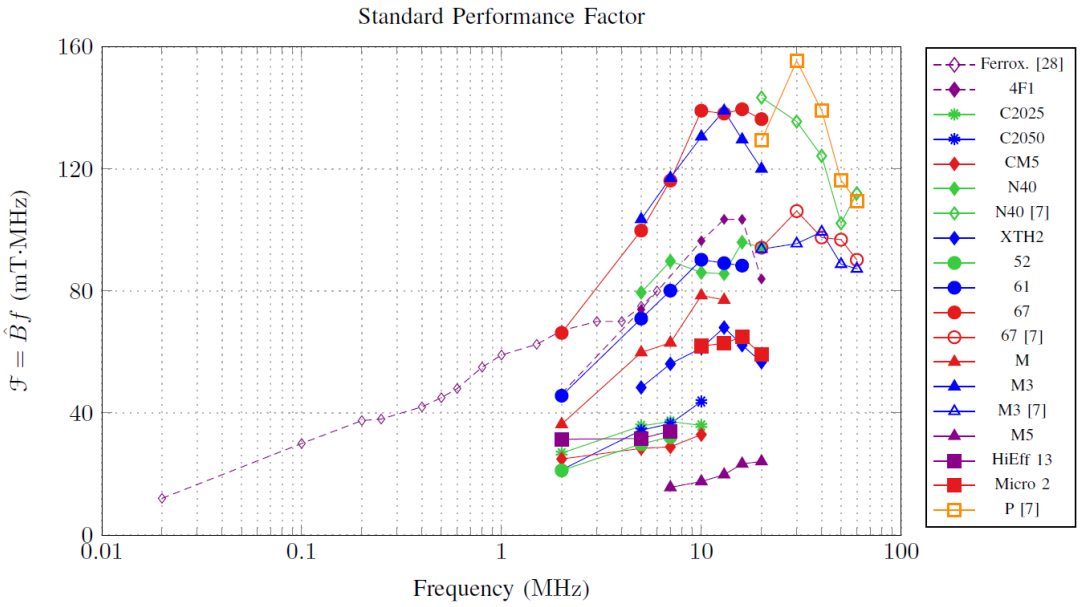


Figure 36 Performance Factor comparison of different materials. Image taken from [10].

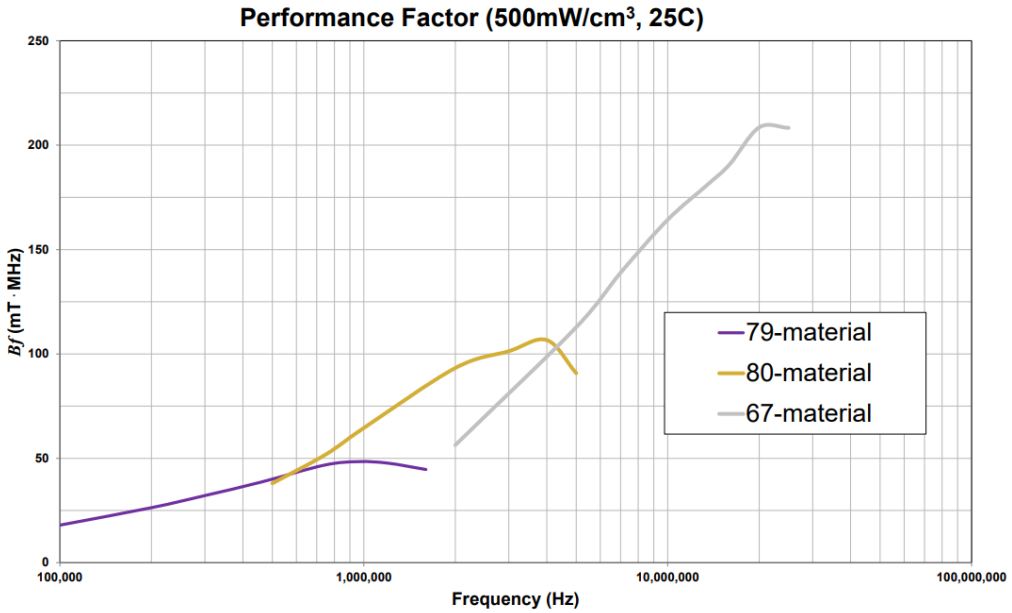


Figure 37 Performance Factor comparison: Material-80, Material-67 and Material-79. Image taken from [11].

# Chapter 4: An Example Design with $L_{mag}$ =105nH, 1-10 Turns Ratio

Using the design guidelines proposed and the trade-offs explored in the previous chapter, a transformer with quasi-distributed gaps was designed for use in a coupled-inductor based boost converter. A high step-up transformer, operating at multi-MHz frequencies and carrying large currents in the windings is ideal to demonstrate the advantages of using the proposed transformer. In this chapter, we explain the steps for constructing a prototype and present a test plan for the same. The simulations showed that the designed transformer achieved the low loss and low leakage inductance properties of the QD gapped transformer presented in the Chapter 2.

## DESIGN CONSTRAINTS

Figure 38 shows the circuit schematic of a coupled-inductor boost converter. The power converter is rated at 400W and steps-up 20V to 400V. It operates at a switching frequency of 2MHz and requires a transformer with a magnetizing inductance of 105nH and a 1-10 turns ratio. The expected peak primary current is 60A. Waveforms of the currents in the two windings are shown in Figure 23.

The constraints on the transformer present significant design challenges which can be successfully mitigated by the proposed transformer structure. Because the transformer carries large primary currents (60A peak), current crowding in the conductors will significantly limit the efficiency of the converter. The proposed structure maintains double sided conduction in all the turns because of which the conduction losses due to current crowding can be eliminated. The reduction in conduction losses is achieved without the use of litz wire. In the absence of a snubber, the power losses due to the stored energy in the leakage inductance of the transformer are significant. For example, a leakage to magnetizing inductance ratio of 5% results in a 7.5% drop in the efficiency of

the converter. Hence, the transformer needs to have as small of a leakage inductance as possible. The primary and secondary turns of the transformer can be interleaved to reduce the leakage inductance. However, as explained in Chapter 2, interleaving of the paralleled turns does not help in reducing the conduction losses in a conventional transformer structure because most of the current flows through the turn closest to the airgap. In the proposed structure however, the ability to split the primary winding in 10 parallel turns, and achieve almost uniform current division amongst them, can be leveraged to reduce the conduction losses as well as leakage inductance. Hence, the coupled-inductor boost converter provides an ideal testing platform for the proposed transformer.

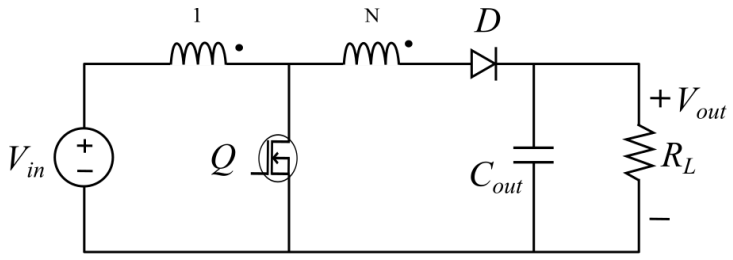


Figure 38 Circuit schematic of a coupled-inductor boost converter.

**DESIGN AND SIMULATIONS IN ANSYS-MAXWELL**

The transformer volume was initially constrained to be equal to the volume of a cylindrical structure with $r_t = 0.5\ [in]$ and $h_t = 1\ [in]$. The height of the endcaps was later tuned to reduce the core losses considering its tradeoff with volume. The primary and secondary windings had one and ten series turns, respectively. The primary was implemented with 10 paralleled turns that were interleaved and paired up with the secondary turns as explained in Chapter 2. The structure thus had 11 air gaps with the air gaps at the endcap having half the length ($l_{g_{ec}} = 50\mu m$) of air gaps in the middle portion

($l_{g_m} = 100\mu m$). To have conduction loss be approximately equal to core loss, we chose a 3:2 aspect ratio. The details of the geometry are provided in Table 7.

Table 7 Geometry and specifications of the simulated transformer

| | |
|---|---|
| Magnetizing Inductance | 105 nH |
| Current | As shown in Figure 23 |
| Core material | Material-80 |
| Total Diameter | 23 mm |
| ▪ Center-post diameter | 15.6 mm |
| ▪ Window width | 2.1 mm |
| Total Core Height | 34.5 mm |
| ▪ Core Section Height | 2.5 mm |
| ▪ Endcap Height | 3.5 mm |
| ▪ Total Gap length | 1 mm |
| Number of Primary turns | 1 series, 10 parallel |
| Number of Secondary turns | 10 series, 1 parallel |
| Wire | 17 AWG |
| ▪ Bare copper diameter | 1.15mm |
| ▪ Total diameter | 1.22 mm |

As seen from Figure 26 and Figure 27 vertical fill of ~90% is optimum for minimizing the conduction losses. A 17AWG, solid magnet wire with heavy duty insulation [12] was used for both primary and secondary windings. Double sided conduction leads to optimum utilization of the skin of the conductor and maximizes the

efficiency obtained for a solid conductor. Not using litz wire leads to a design with reduced cost. The insulation coating on the wire provided the required spacing between the conductors. For ease of construction, the spacing between the conductors of primary and secondary windings of a pair ($c_s$) and the spacing between adjacent pairs ($p_s$) was kept equal. The winding achieved a vertical fill of ~88.5%. Material-80 was chosen as the core material due to its superior performance at 2MHz as compared to most of the available core materials on the market. For a window width of 2.1mm and the chosen wire diameter, the horizontal fill is ~55%. From Figure 32, it can be seen that the chosen window width minimizes the total losses for a transformer with 3:2 aspect ratio. The outer-shell has two vertical windows of width 3.9 mm through which the winding terminals can connect to the printed circuit board. An extra layer of core sections was added to accommodate the helical shaped winding.

"Eddy current" simulations were performed in ANSYS Maxwell to find the inductance matrix parameters and the H, B and J field plots. These plots are shown in Figure 41 – Figure 42. The transformer achieves double sided conduction because of the balanced H-fields on the two sides of the winding. The inductance matrix parameters obtained from FEA simulations are shown in Table 8. These 2-D FEA simulations do not include the vertical windows leading to a magnetizing inductance larger than 105 nH. The expected leakage to magnetizing inductance percentage, as calculated from the inductance matrix, is ~0.8%. From Figure 41 it can be seen that the current divides almost evenly in the paralleled turns and flows along the entire skin of the conductor. The expected average conduction and core losses found from transient simulations are ~0.72 W and ~0.4 W, respectively.

Table 8 Impedance matrix of the simulated transformer

| | | | |
|---|---|---|---|
| $R_{11}, L_{11}$ | $1(m\Omega)$, $113.75(nH)$ | $R_{12}, L_{12}$ | $1.1346(m\Omega)$, $1132.8(nH)$ |
| $R_{21}, L_{21}$ | $1.1346(m\Omega)$, $1132.8(nH)$ | $R_{22}, L_{22}$ | $95(m\Omega)$, $11372(nH)$ |

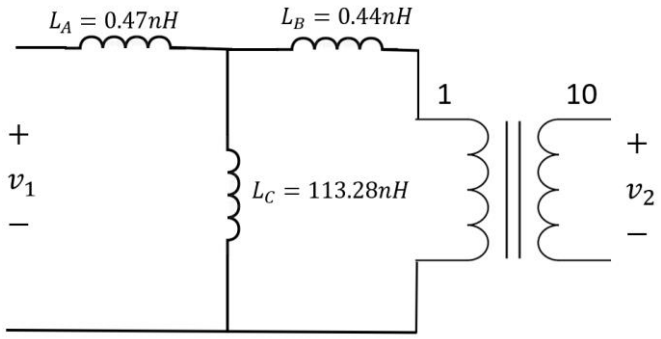


Figure 39 Equivalent circuit of the transformer based on the inductance matrix values obtained from ANSYS Maxwell simulation.

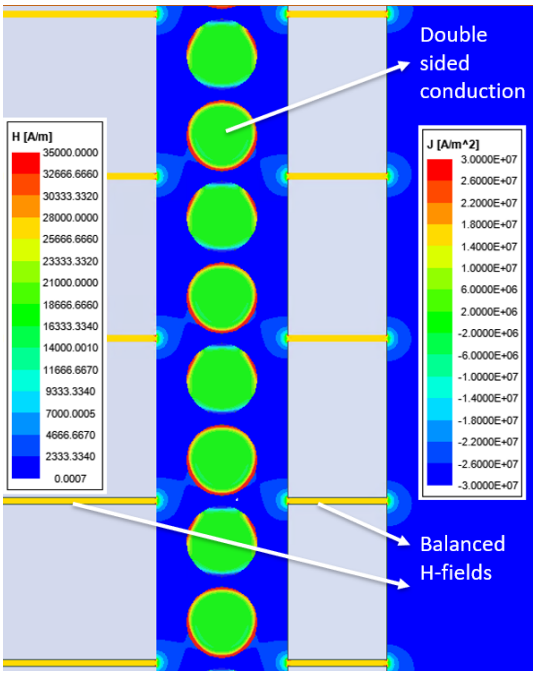


Figure 40 Balanced H-fields on the two sides of the winding.

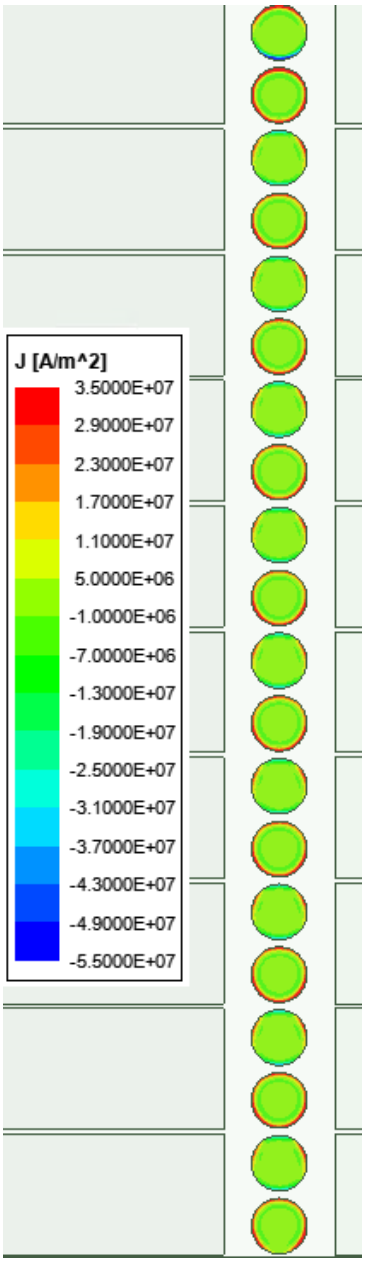


Figure 41 Current distribution in the windings. The winding maintains double sided conduction in all the turns.

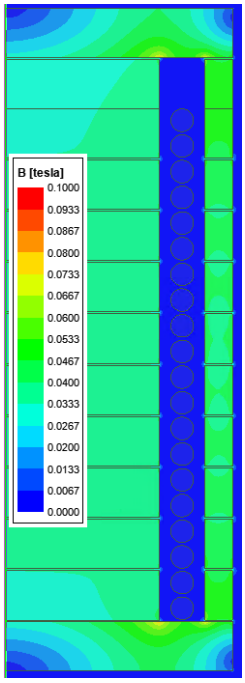


Figure 42 B-field in the core. Balancing the H-field in the center-post and outer-shell leads to an almost uniform distribution of B-field in the core.

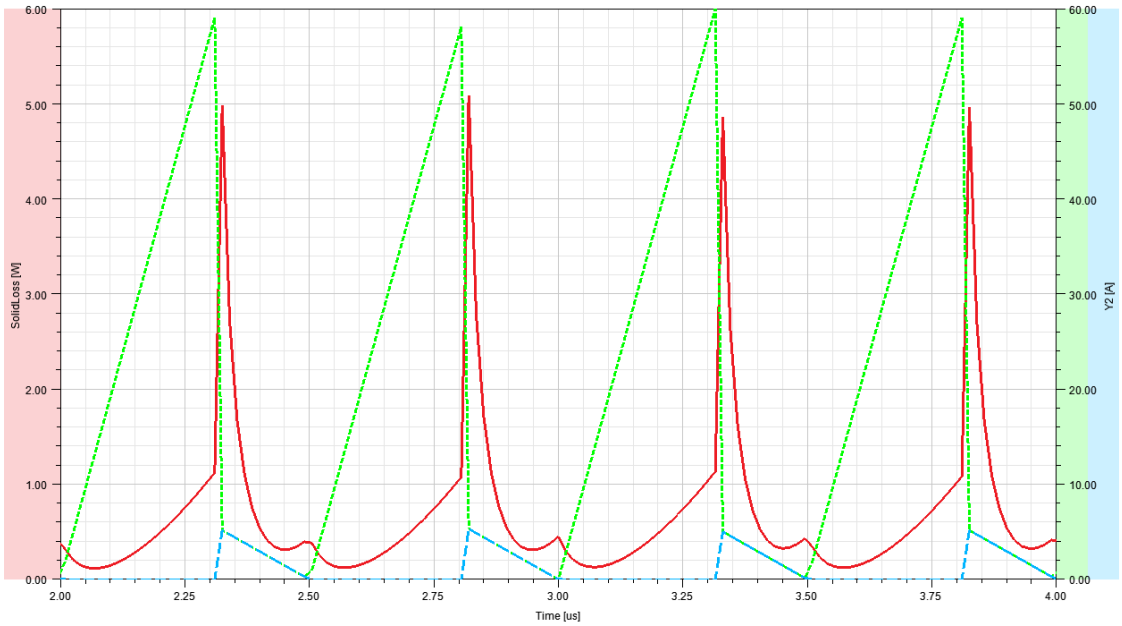


Figure 43 Current waveforms in the primary winding (green), secondary winding (blue) and solid loss in the winding (red). Average solid loss = 720mW.

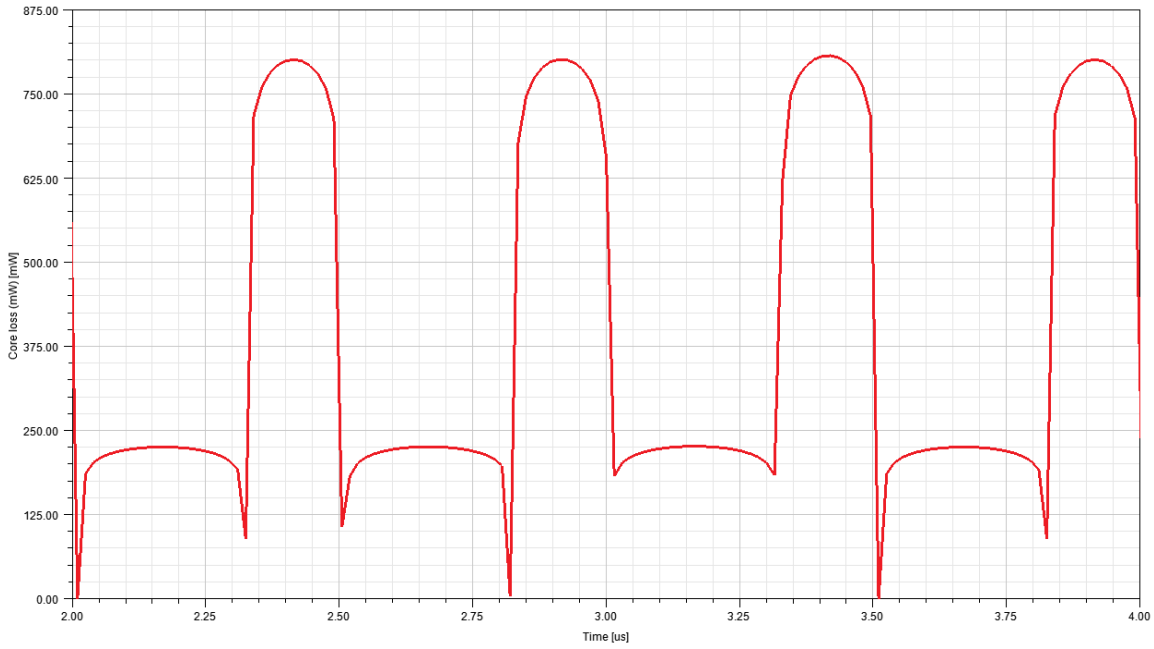


Figure 44 Total core loss in the transformer (average = 403mW). Average core loss in center-post, outer-shell and endcaps was 176mW, 151mW and 75mW respectively.

To build the transformer, core pieces made out of Material-80 were custom built. Because they had to be custom manufactured, there was a significant lead time, and the core pieces were not received within the time limit of the thesis. Here we demonstrate the steps involved in constructing the prototype using 3D printed pieces made from plastic. Later, we discuss the proposed testing plan for the transformer to validate the simulations performed in ANSYS Maxwell. Many works in the literature have used ANSYS Maxwell to demonstrate the validity of their magnetic structure and the experimental results matched the simulation results [7, 24 -33].

## PROTOTYPE CONSTRUCTION

We propose the following steps to build the transformer structure. First, the core material needs to be cut into the desired shapes. The two endcaps and each section of the

center post can be made out of thin discs of the desired height and radius. A stack up of the desired number of C-shaped core pieces can make up one half of the outer shell. Figure 45 to Figure 47 show the drawings of the core pieces that were manufactured.

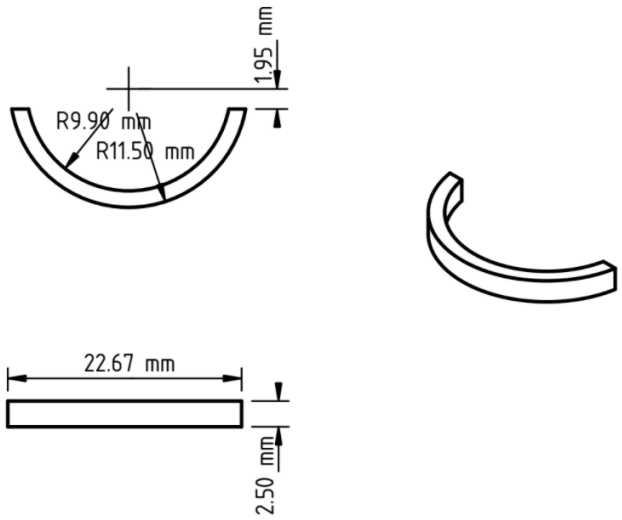


Figure 45 Drawing of a C-shaped piece of the outer shell that was manufactured. Eleven such pieces will be stacked (with laser cut pieces of shim stock providing the airgap spacing) to form one half of the outer shell.

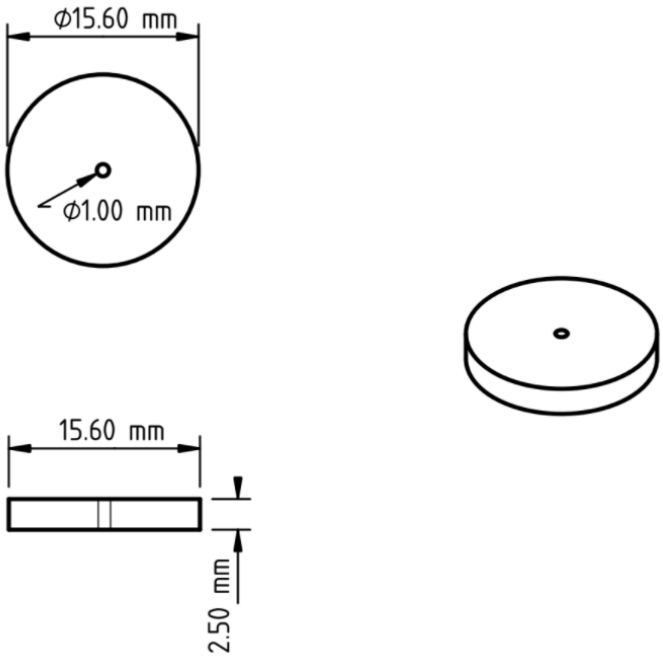


Figure 46 Drawing of piece of the center post that was manufactured. Eleven such pieces will be stacked (with laser cut pieces of shim stock providing the airgap spacing) to form the center post.

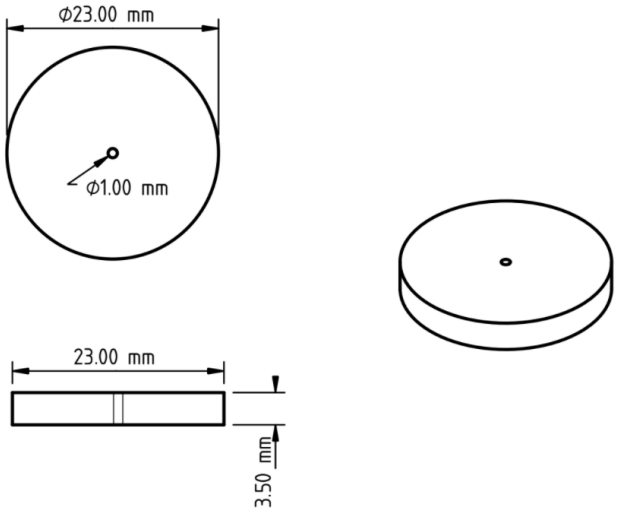


Figure 47 Drawing of an endcap that was manufactured.

Figure 50 – Figure 53 demonstrate the recommended procedure for constructing the prototype. The dummy prototype model was built modularly. The center post was made by stacking the core pieces together. A rod with 1mm diameter was inserted through a similarly sized hole in the center of the center-post pieces and endcaps to align them properly. The quasi-distributed gaps were created by placing pieces of shim-stock of appropriate thickness between the core pieces. The shim-stock was laser cut into the desired shapes. After assembling the center post, it was vertically pressed and taped so that it maintained its shape. The thickness of the tape was chosen to provide the desired separation between the center post and the winding.

The winding was made such that 10 turns of the primary were paralleled and interleaved with the secondary turns. Figure 48 shows the winding pattern. To assist in winding the wire, a jig was 3D printed. The winding was first wound on the jig and then removed and placed around the center post. The 10-turn secondary was first tightly wound on the jig while leaving space for a primary turn to be wound between two adjacent secondary turns. Primary turns were wound one at a time and each turn was glued with the secondary turns on its either side so that it remained in place. Care was taken to leave minimum amount of space between the secondary and primary turns. Figure 49 shows the winding and the fixture. Each primary turn starts from one layer and ends on the layer above it (see Figure 48). For example, the first turn starts on the bottom left and ends on the right side on the second layer. The second paralleled turn of the primary starts on the left of the end terminal of the first turn. Once all turns were wound, the winding was slid out from the jig and inserted around the center post. It was then covered with more layers of tape to provide the spacing between the winding and the outer shell.

The outer shell was created by stacking C-shaped core pieces on a 3D printed fixture as shown in Figure 52. The C-shaped core pieces and the laser-cut shim-stock pieces were mounted on the jig, pressed tightly and then taped. This was repeated to generate the other half of the outer shell. These separate sections of the outer shell were then placed around the center post and the winding. Figure 50 - Figure 53 show the prototype in different stages of construction. The final prototype was wrapped with tape to apply vertical pressure. This can now be soldered on a PCB for testing.

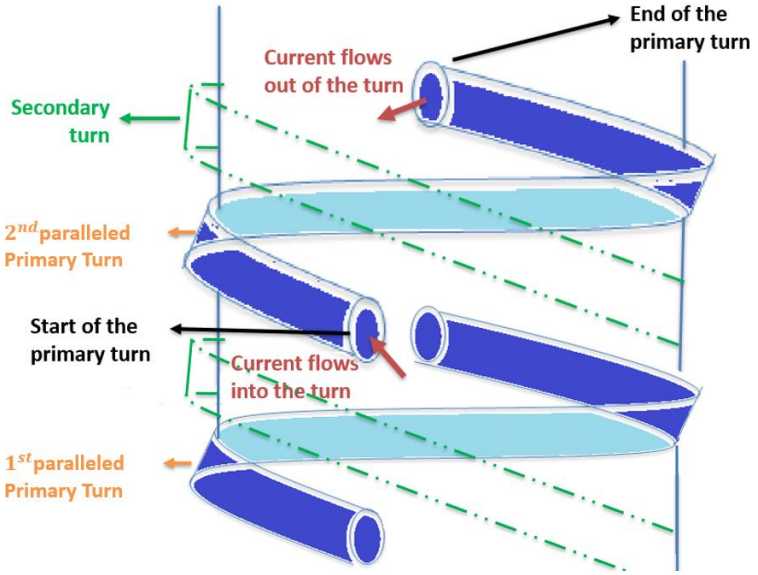


Figure 48 Winding pattern for the primary and secondary turns.

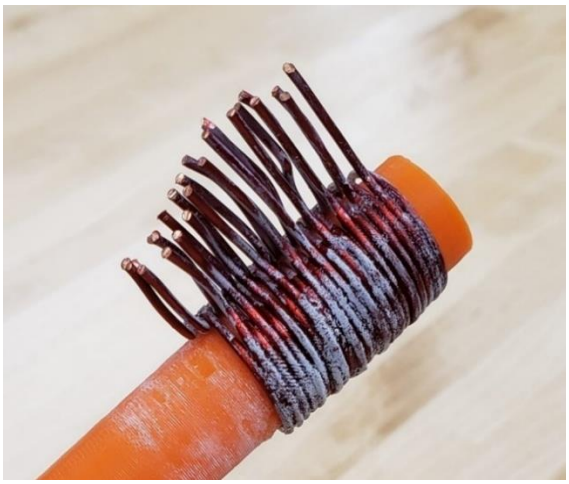

Figure 49 Winding wound on a 3D printed jig. The primary has 10 paralleled turns that are interleaved with secondary (as shown in Figure 48). Each turn is glued to adjacent ones so that it maintains its shape.

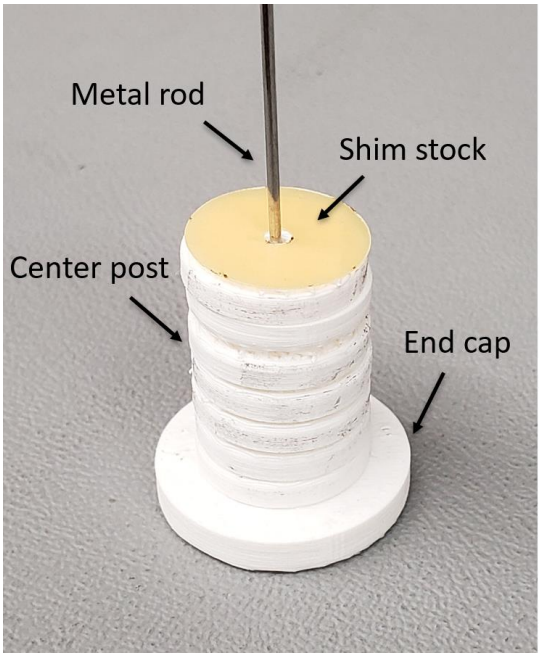


Figure 50 Center post pieces made out of plastic being assembled. A metal rod helps in alignment. Laser cut pieces of shim stock used to provide an air gap.

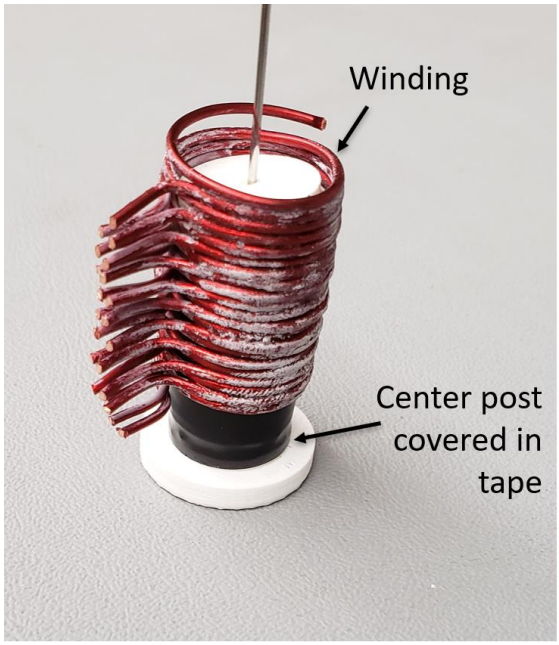


Figure 51 Winding being inserted on the assembled center post.


Figure 52 Outer shell pieces being mounted on a jig. Laser cut shim stock pieces provide the airgap.

Figure 53 Assembled structure was covered with multiple layers of tape to apply vertical pressure.

## TEST PLAN

Appendix C shows the complete layout of the PCB that has been designed to test the transformer. The layout of the test circuit alone is shown in Figure 54 with the loops on the PCB highlighted. Care was taken to have minimum loop inductance in the layout. Following tests will be performed to validate the performance of the transformer.

### Finding the inductance matrix

The prototype transformer will be tested using an Impedance Analyzer (E5061B from Keysight). The T-model parameters can be found from the inductance matrix by the following relations.

$$L_A = L_{11} - NL_{12}$$

$$L_B = N^2 L_{22} - NL_{12}$$

$$L_C = NL_{12}$$

Here, $L_A$ is the leakage inductance on the primary side, $L_B$ is the primary-referred secondary leakage inductance and $L_c$ is the magnetizing inductance. $N$ is equal to $N_1/N_2$.

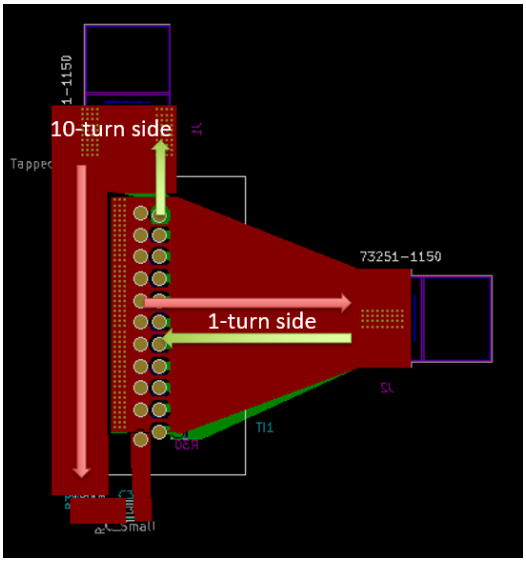


Figure 54 Layout of the test circuit with loops highlighted.

Table 9 Recommended measurements to identify parameters of the inductance matrix.

| | Port 1 | Port 2 | Measure |
|---|---|---|---|
| 1 | Apply $v_1$ | Open Circuit | $Z_1/j\omega = L_{11}$ |
| 2 | | | $\frac{v_2}{v_1} = \left(\frac{NL_{12}}{L_{11}}\right)\left(\frac{1}{N}\right) \rightarrow L_{12} = L_{11}\left(\frac{v_2}{v_1}\right)$ |
| 3 | Open Circuit | Apply $v_2$ | $Z_2/j\omega = L_{22}$ |

**Determining current sharing between paralleled turns**

To test how well the current distributes in the paralleled turns of the transformer, the 1-turn side can be excited till the winding carries the desired amount of current. Sensing resistors can be used to measure the current through the turns. The choice of resistance is a trade-off between the voltage obtained across it (larger voltage can be measured with more fidelity) and the effect it has on current sharing between the turns. To quantify the effect of resistance value on current sharing, simulations were performed

in ANSYS Maxwell with the resistors included in ANSYS SchematicEditor. Table 10 shows currents through the turns when different resistances are used. Considering these trade-offs, five sensing resistors of 0.5Ω, 1W are included on the PCB on the 1-turn side such that each resistor will carry a combined current from two paralleled turns. Using one resistor for sensing current through two turns allowed implementation of a PCB layout with lower parasitic inductances.

Table 10 Current distribution among turns in the presence of $R_{sense}$ when 10-turn side was excited with 10A.

| $R_{sense}$ | Turn 1 | Turn 2 | Turn 3 | Turn 4 | Turn 5 | Turn 6 | Turn 7 | Turn 8 | Turn 9 | Turn1 0 |
|---|---|---|---|---|---|---|---|---|---|---|
| 0Ω | 0.858 | 1.012 | 0.981 | 0.962 | 0.951 | 0.948 | 0.952 | 0.964 | 0.987 | 1.381 |
| $20m\Omega$ | 0.858 | 1.013 | 0.98 | 0.961 | 0.952 | 0.948 | 0.953 | 0.969 | 0.982 | 1.381 |
| 0.5Ω | 0.86 | 1.031 | 0.965 | 0.955 | 0.962 | 1.004 | 0.9 | 1.152 | 0.795 | 1.374 |

**Determining core loss**

One possible way of determining that the winding experiences double sided conduction is by comparing the conduction loss measurements from ANSYS Maxwell with the experimental results. This, however, is not straightforward because the total power loss measured in the experimental results includes both core and conduction losses. Even though comparing the total power loss from the simulation and experimental setup could be sufficient to quantify the transformer's performance as a whole, being able to separate the core and copper losses will provide a more direct proof of double-sided conduction. We thus also include circuitry to allow core loss measurement in the setup. While different methods are proposed in the literature for measuring core loss ([20] [22])

each method has some challenges and limitations. Method suggested in [20] is sensitive to the phase discrepancy in the measured current and voltage waveforms as explained in [23]. Trying to estimate the winding resistance from an air core structure as recommended in [22] could be challenging in the presence of airgaps in the transformer under test [21].

The method recommended in [23] has low sensitivity to the phase difference between the current and voltage and does not require finding the winding resistance. Figure 55 shows the circuit schematic. A capacitor ($C_r$) is used to resonate with the magnetizing inductance ($L_m$) because of which the voltages $v_{L_m}$ and $v_{C_r}$ cancel each other. The voltage on the secondary, $v_2$, is ($v_{R_{core}} + v_{L_m}$) scaled by the turns-ratio. One advantage of using this method is that $v_2$ does not include the voltage drop due to the winding resistance, allowing us to isolate core loss. By adding $v_{C_r}$ to an appropriately scaled value of $v_2$ we can find $v_{R_{core}}$. The current through the winding can be found either from the voltage and impedance information of the capacitor or by using a sensing resistor. The current and $v_{R_{core}}$ will be in phase and can be used to find the core loss in the system without much sensitivity to the errors in phase measurements. Core loss can be calculated by the below equation [23].

$$P_{core} = \frac{1}{TR_{sense}} \int_0^T v_{R_{sense}} v_{R_{core}} dt$$

A $560pF$, 500V rated, high Q capacitor was selected to be used for establishing the resonance. If the magnetizing inductance referred to the 10-turn side is $10.5\mu H$, the capacitor will resonate with the inductor at ~2.075MHz. After finding $P_{core}$ the winding loss can be found and compared with the simulation results.

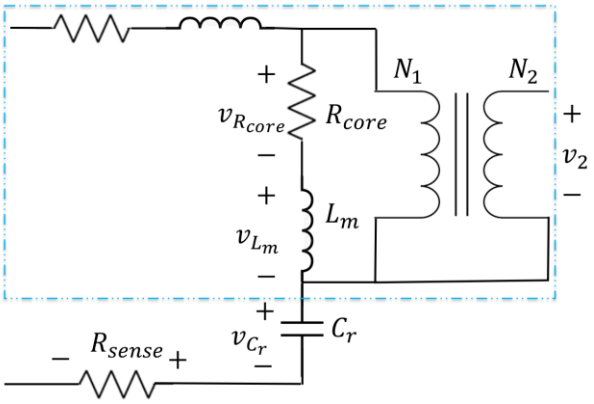


Figure 55 Core loss measurement circuitry with equivalent model of the transformer[23]

**Performance in the coupled-inductor boost converter**

Finally, the transformer will be tested in the coupled-inductor boost converter. Appendix C shows the layout of the converter. Simulations of the coupled inductor boost converter were performed in PLECS software with a conventional lumped gap transformer (assuming 5% leakage to magnetizing inductance) and with the proposed transformer (with inductance matrix values obtained from ANSYS Maxwell – shown in Table 8). The converter efficiency improved substantially, from 92% to 98%, when the proposed transformer was used instead of the conventional transformer. The improvement in the efficiency of the converter when using the proposed transformer will be experimentally validated and compared with that when a conventional transformer is used. Figure 56 shows a conventional pot core transformer that was built with a winding interleaved in the manner shown in Figure 48.

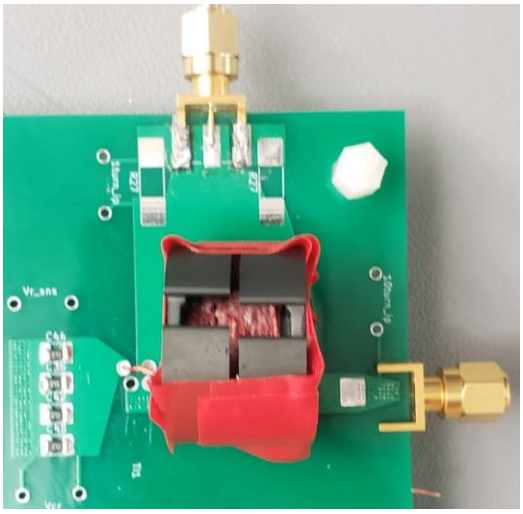

Figure 56 A conventional pot core transformer (1-10 turns, $L_{mag} = 105nH$) built for comparison with the proposed transformer structure.

# Chapter 5: Conclusion

In this thesis we proposed a low loss, low leakage transformer that is suitable for application in high frequency power converters. The proposed structure achieves almost zero MMF drop across the window reluctance ($R_w$). Because of this, the transformer achieves a very small leakage inductance. Low leakage inductance enables the use of this transformer structure in power converters like coupled-inductor boost or Flyback converters which would otherwise require additional circuitry to recover the energy stored in the leakage inductance. The transformer achieves low conduction losses by balancing the H-fields on the two sides of the windings so that the current flows along nearly the entire skin of the conductor. Quasi-distributed gaps and balanced H-fields result in each turn of the transformer winding being in a magnetically similar environment. This allows paralleling of the turns of the transformer winding such that each turn carries almost equal current. These properties make the transformer especially suitable for applications with large currents and requiring high turns ratio.

The analytical method and formulae for finding the airgap reluctances and the leakage and magnetizing inductances can be used to solve the reluctance model of the structure either in a Spice simulator like LTSpice or by solving the circuit equations in an appropriate scripting language like MATLAB. Being able to predict the performance of the structure without relying on the much slower Finite Element Analysis methods helps speedup the design process. The design guidelines provided in the thesis further help in identifying crucial design tradeoffs. Using the recommended values of the design parameters helps in achieving a roughly optimized transformer. The designer can then choose to refine the design by running FEA simulations. The proposed design guidelines were used to design a transformer to be used in a coupled inductor based boost converter.

# Appendices

## APPENDIX A: SIMULATION SETUP

In Chapter 3, Design Guidelines, core and conduction losses were found using ANSYS Maxwell. Here, we briefly discuss the method used to find the same.

For a chosen Horizontal and Vertical Fill, the center-post, outer-shell and the airgaps were sized to achieve the desired magnetizing inductance and balanced H-field on the two sides of the winding. Eddy current simulations were used to obtain the inductance matrix and study the H, B and J-Fields in the structure. Both primary and secondary turns were excited externally through ANSYS Schematic Editor. After finalizing the structure that achieved the desired impedance matrix and double-sided conduction, a transient simulation was setup with the same structure and a piecewise-linear current excitation shown in Figure 23. This transient simulation was used to determine the core and winding losses in the transformer.

Winding losses can be found analytically using the resistance matrix parameters as shown below [13].

$$P_{av} = 0.5|I_1|^2 R_{11} + 0.5|I_2|^2 R_{22} + |I_1||I_2| R_m \cos\left(\angle I_1 - \angle I_2\right) \qquad (28)$$

Here, $I_1$ and $I_2$ are the primary and secondary current phasors. For a non-sinusoidal current waveform, the total conduction loss ($P_{av}$) can be found by summing up the power loss due to currents of each harmonic. Even though it is possible to break up the primary and secondary current waveforms of Figure 23 into their constituent harmonics and calculate the power loss from the magnitude and relative phase information of each harmonic, finding conduction loss through transient simulations is a quicker way for doing the same. In ANSYS Maxwell, the average “solid loss” over one

cycle can be plotted and the average of the same was used as an estimate of the conduction loss per cycle.

Unlike conduction losses, finding core loss for a non-sinusoidal excitation using analytical methods is not straight forward. Both, the Steinmetz Equation and the power loss density data provided by manufacturers are based on sinusoidal excitation. However, like in our case, magnetics in power converters often experience non-sinusoidal excitations. The Steinmetz Equation also does not consider the effects of DC bias in the excitation waveform and minor loops in the same [14]. All these things make the use of Steinmetz Equation to predict the core loss less reliable. In addition to this, the distribution of the magnetic field in the core is not uniform. Because of this, simply using the average value of the B-field in the entire core in core loss equations, like Steinmetz Equation, will not yield a correct answer even for a sinusoidal excitation.

The core loss feature in ANSYS Maxwell should consider the non-uniform distribution of the B-field in the core. The author, however, is not aware of the methods the core loss function uses to determine the losses in a transient simulation with non-sinusoidal excitation. We, thus, compare the core loss results obtained from ANSYS Maxwell's core loss function with the core loss predicted by "improved Generalized Steinmetz Equation" (iGSE). iGSE is a commonly employed analytical method for estimating core loss in the presence of a non-sinusoidal excitation and its predictions have been shown to agree well with experimental results [15].

To find core loss using iGSE, one needs to know the magnetic flux density (B) as a function of time. Considering average B-field in the center-post and finding losses in it is better for comparing ANSYS Maxwell's loss calculations with iGSE instead of considering the entire structure because the center-post has an almost uniform B-field distribution. An example plot of average B-field in the center-post is shown in Figure 57.

As can be seen, for the current excitation of Figure 23, the B-field plot does not have minor loops. Core loss using iGSE was found by numerically solving equations (29) and (30) using a MATLAB script [15]. $k, \alpha$ and $\beta$ are the Steinmetz Parameters found from the power loss density data provided by the manufacturer.

$$P_v = \frac{1}{T}\int_0^T k \left|\frac{dB}{dt}\right|^{\alpha} (\Delta B)^{\beta-\alpha} dt \tag{29}$$

$$k_i = \frac{k}{(2\pi)^{\alpha-1}\int_0^{2\pi} |cos\theta|^{\alpha} 2^{\beta-\alpha} d\theta} \tag{30}$$

To find core loss in ANSYS Maxwell, a new material was defined using the B-H curve and the power loss density curves provided by the manufacturer. For an application which does not experience large peak B-fields a constant permeability can be provided instead. Figure 58 and Figure 59 show the B-H and power loss density data that were input in the material definition window. Based on the power loss density data provided, ANSYS Maxwell automatically calculates the Steinmetz Constants for the material. For the Steinmetz Equation - $P_v(W/m^3) = kf^{\alpha}B^{\beta}$ – the values of $k, \alpha$ and $\beta$ were found to be $1.44 \times 10^{-6}, 2.37$ and $2.54$ respectively. The same constants were used to find core loss using iGSE.

Core loss in the center-post found using ANSYS Maxwell and iGSE agreed with each other to a good extent. From Figure 43 it can be seen that there is ~10% difference between the predictions of the two methods. Having found that the two methods give similar results, further core loss estimates were found using ANSYS Maxwell as it would take the non-uniform distribution of B-field into account.

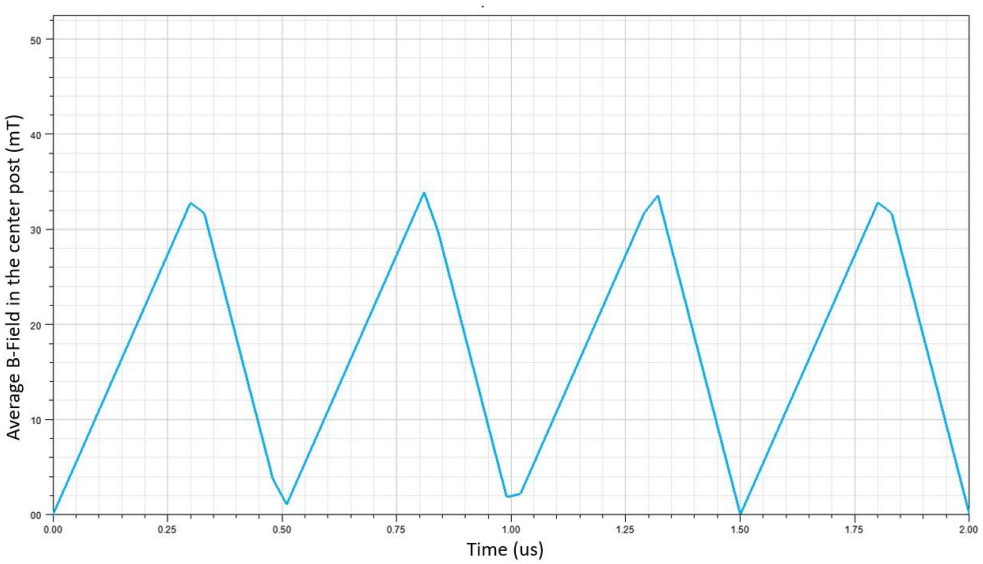


Figure 57 Average B-field in the center-post as a function of time

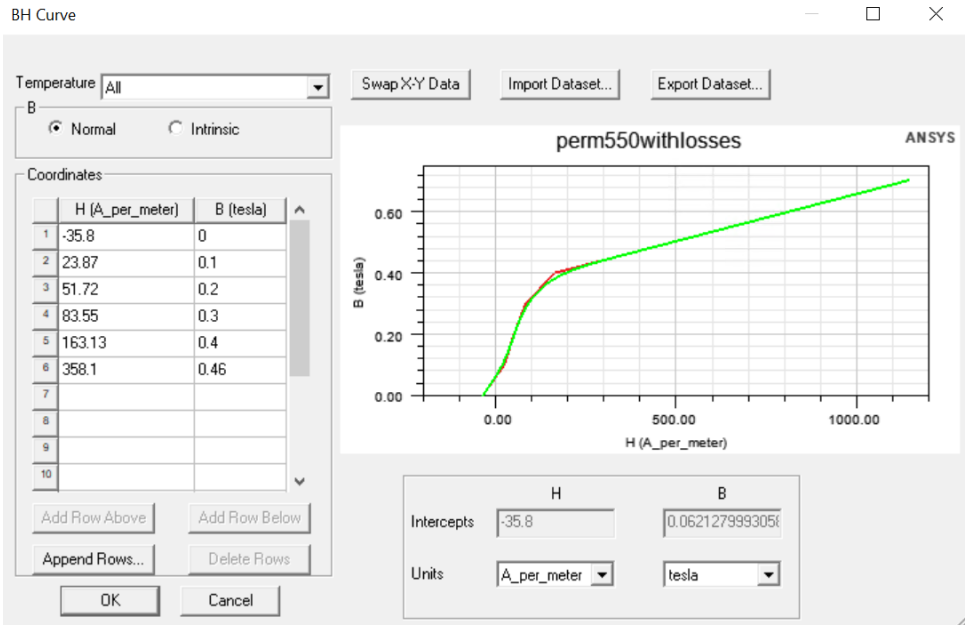


Figure 58 B-H data input to ANSYS Maxwell.

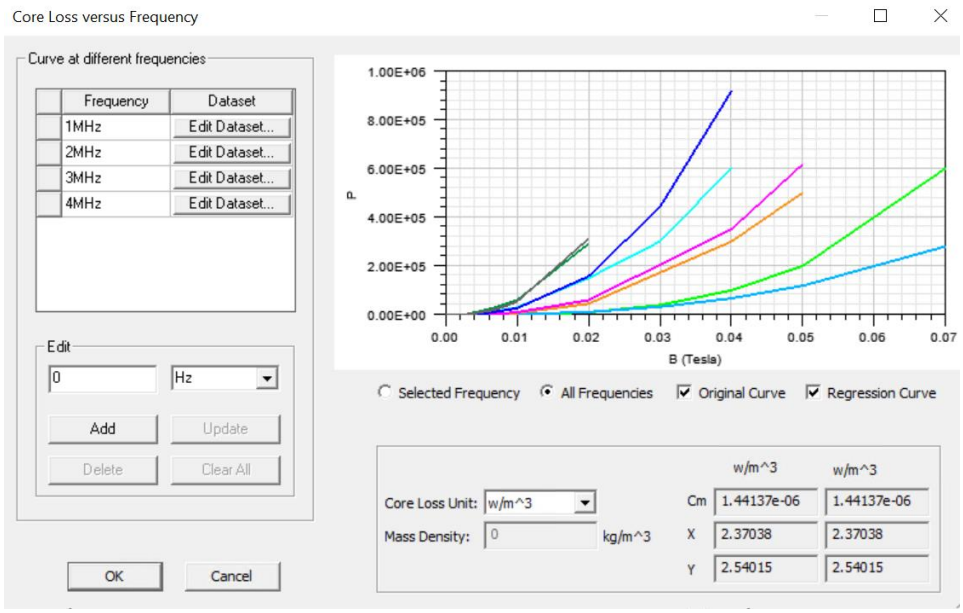


Figure 59 Power loss density at different frequencies input to ANSYS Maxwell.

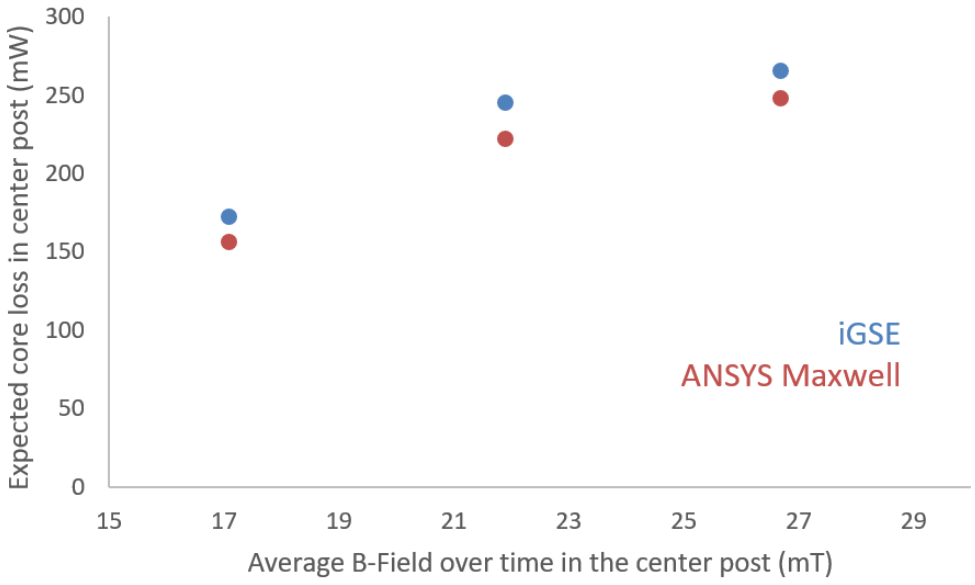


Figure 60 Comparing core loss predictions of Improved Generalized Steinmetz Equation and ANSYS Maxwell

## APPENDIX B: FRINGING FIELD LOSSES FOR THE $F_h$ AND $F_v$ RECOMMENDATIONS IN CHAPTER 3

Here we show that the recommendations of the Horizontal and Vertical Fills for the proposed structure are in agreement with the recommendations of [2] for most parts of the recommended range. To minimize the losses due to fringing fields due to quasi-distributed gaps, [2] recommends that the pitch of the gaps ($p$) and the spacing between the QD gap and the winding ($s$) should satisfy the relation $p < 4s$. The derivation below follows a similar route as in [7].

The horizontal and the vertical fills can be written in terms of the number of turns (N), the wire diameter ($D_w$) and the window height ($h_w$) as follows. The window height ($h_w$) is simply $N \times p$.

$$F_v = \frac{2ND_w}{h_w} = \frac{2ND_w}{Np} = \frac{2D_w}{p} \tag{31}$$

$$F_h = \frac{D_w}{w} \tag{32}$$

The spacing between the winding and the QD gaps can be written in terms of $F_v$ and $F_h$ as below,

$$s = \frac{w - D_w}{2} = \frac{\frac{F_v p}{2F_h} - \frac{F_v p}{2}}{2} \tag{33}$$

[2] recommends $\frac{p}{s} < 4$, thus,

$$\frac{p}{s} = \frac{4}{\frac{F_v}{F_h} - F_v} < 4 \tag{34}$$

Or,

$$\left(\frac{1}{F_h} - 1\right) F_v > 1 \tag{35}$$

Many combinations in the ranges $0.4 < F_h < 0.5$ (lower half of the recommended $F_h$ range) and $0.85 < F_v < 0.95$ (entire recommended $F_v$ range), satisfy the above

criteria. For the edge cases, for example when $F_v$ is small, it is possible to consciously choose $F_h$ to be low to meet the criteria in [2]. For $F_h > 0.5$, however, the recommendations of Chapter 3 will violate the recommendations of [2]. FEA simulations, however, show that despite not meeting the $p < 4s$ criteria, these edge cases still generate nearly optimized structures. It can be seen from Figure 31 that the designs which have their optima at higher $F_h$ also have higher $F_v$. This trend is in agreement with the $p < 4s$ criteria because to satisfy Equation 35 for larger horizontal fill, the vertical fill must also be larger.

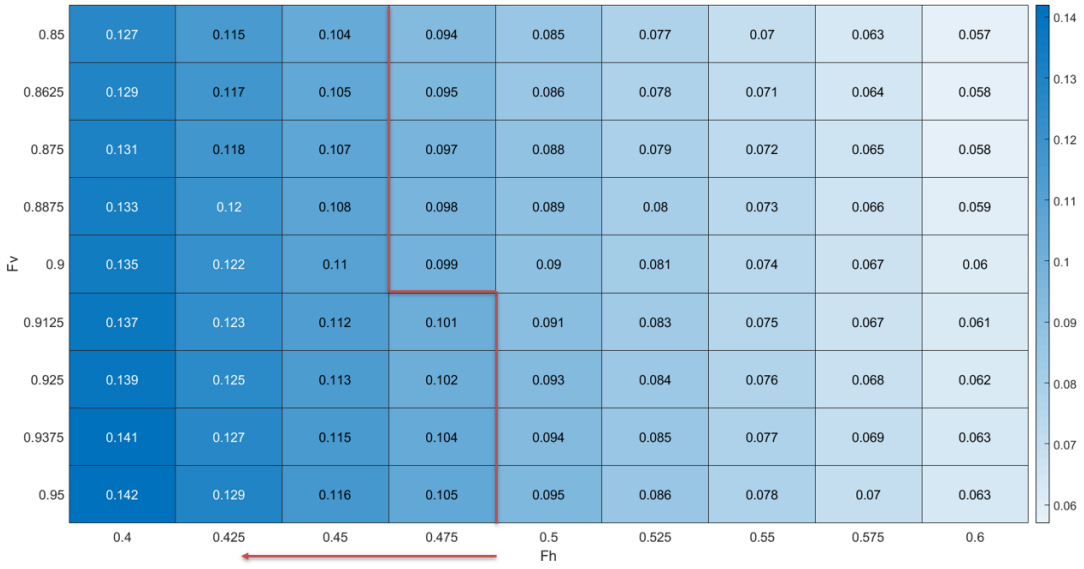


Figure 61 Solutions to Equation 35 for various recommended $F_h$ and $F_v$ values. $F_h$ and $F_v$ combinations to the left of the red line satisfy $p < 4s$ criteria.

## APPENDIX C: LAYOUT OF THE PCB

This appendix contains the PCB layout of the power converter and the testing setup (top left of the PCB). The PCB layout design was largely carried out by Allen Nguyen.

The images are in the following order:

1. Front copper layer
2. Bottom copper layer
3. Copper layer 2
4. Copper Layer 3
5. Front solder mask
6. Bottom solder mask
7. Front silk screen
8. Bottom silk screen

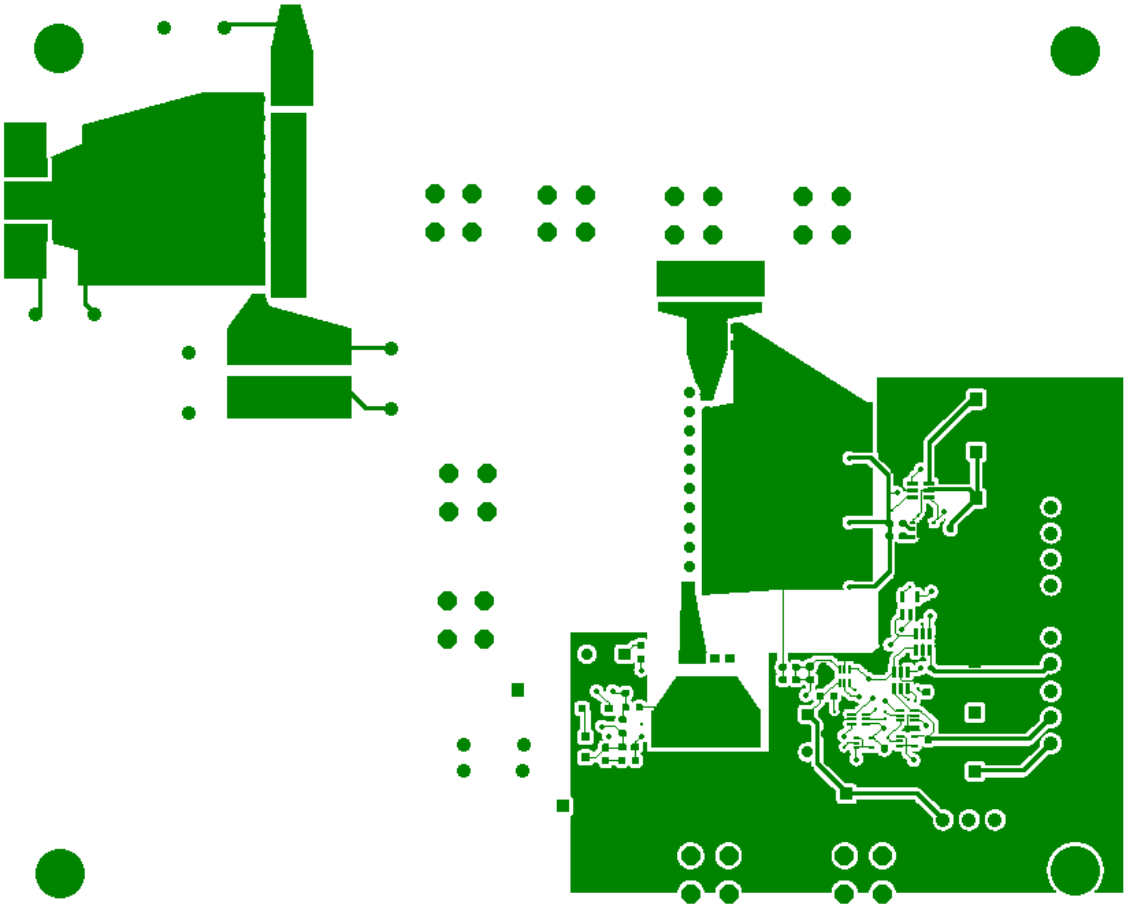

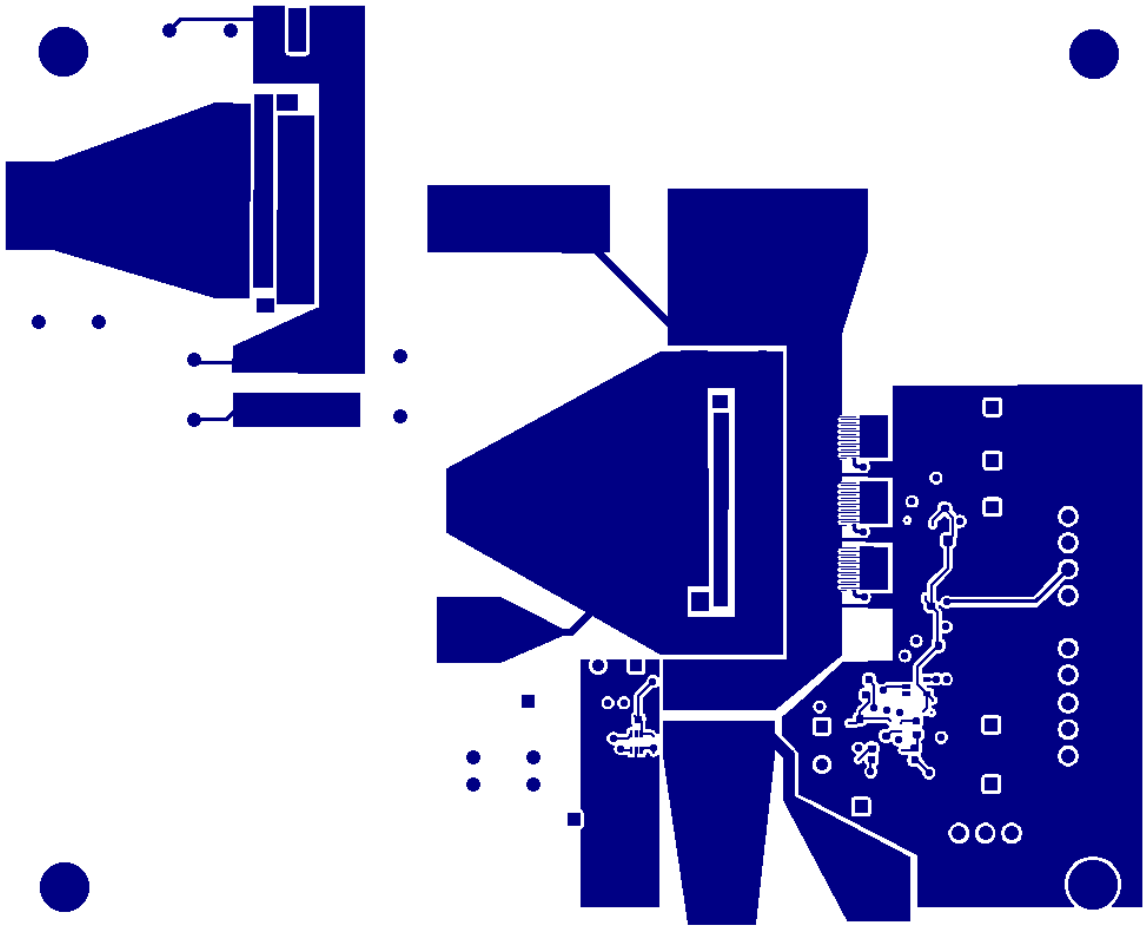

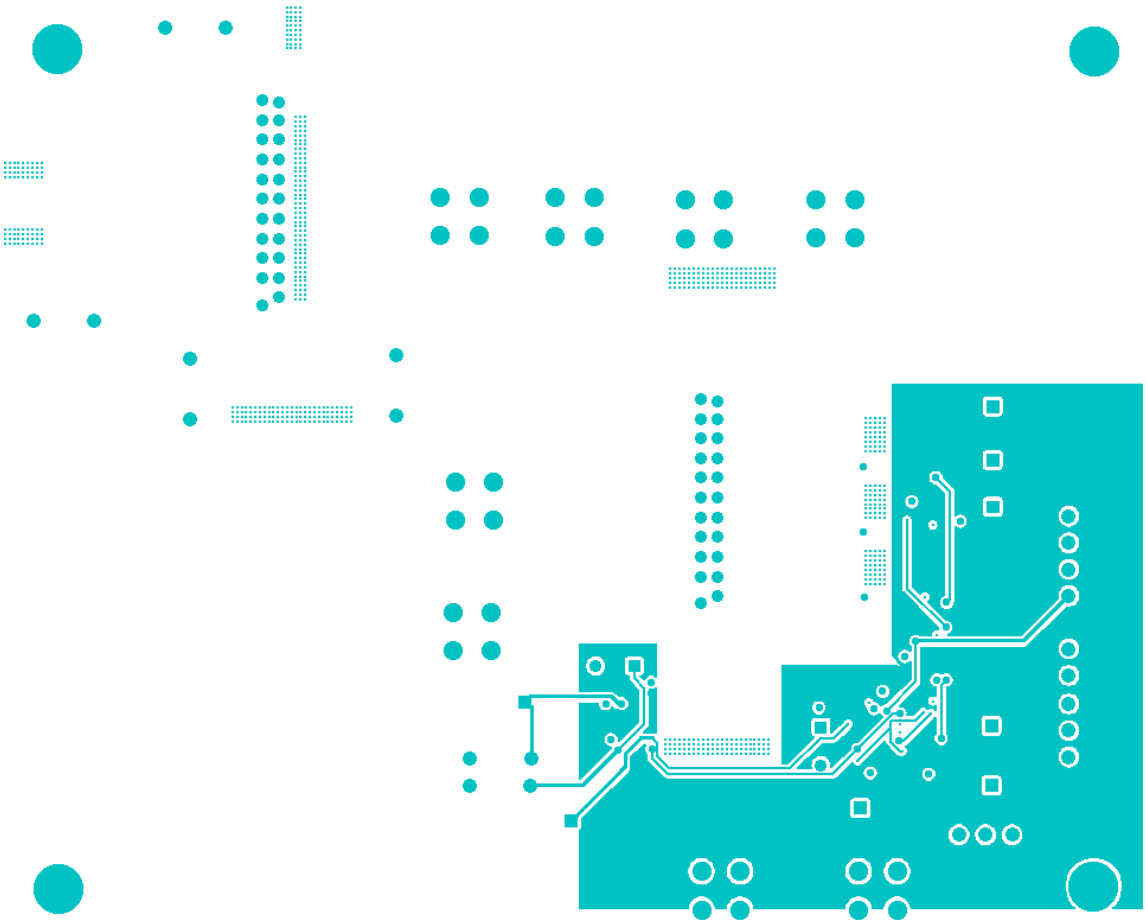

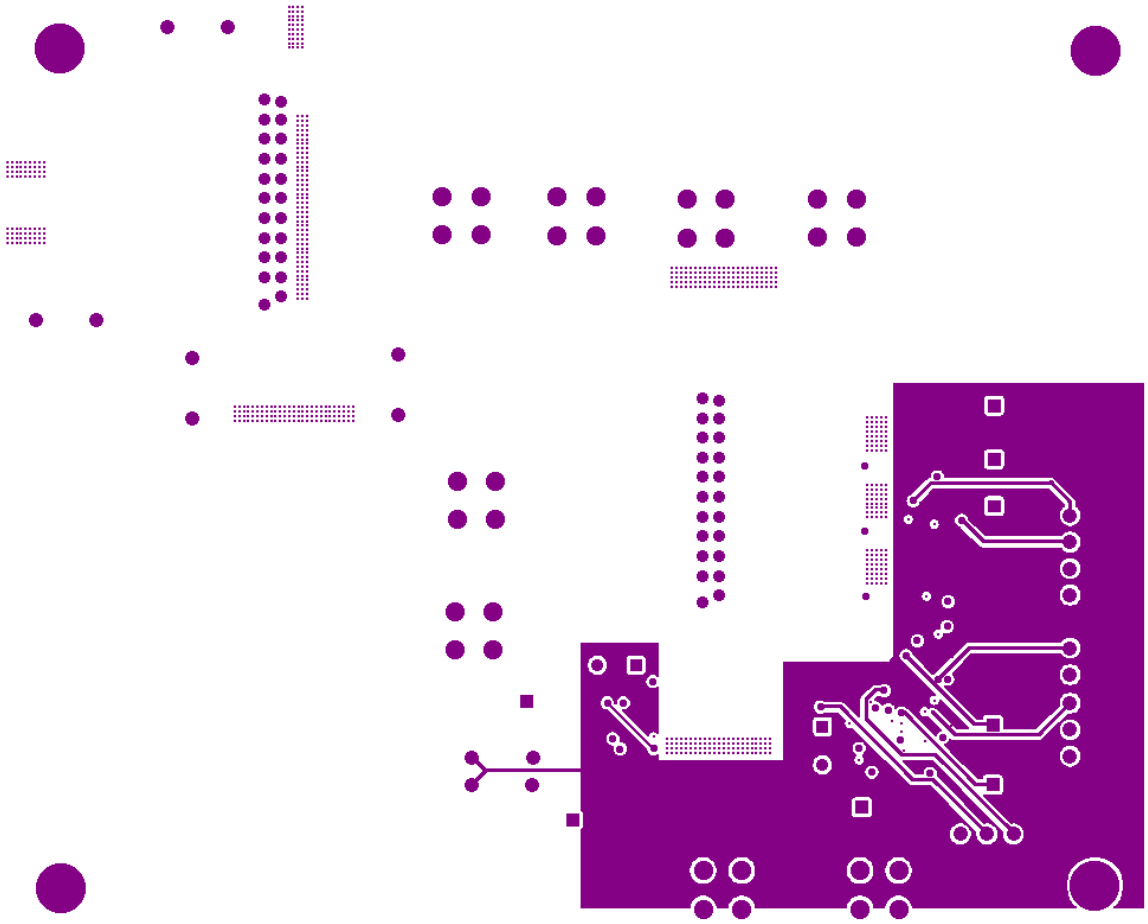

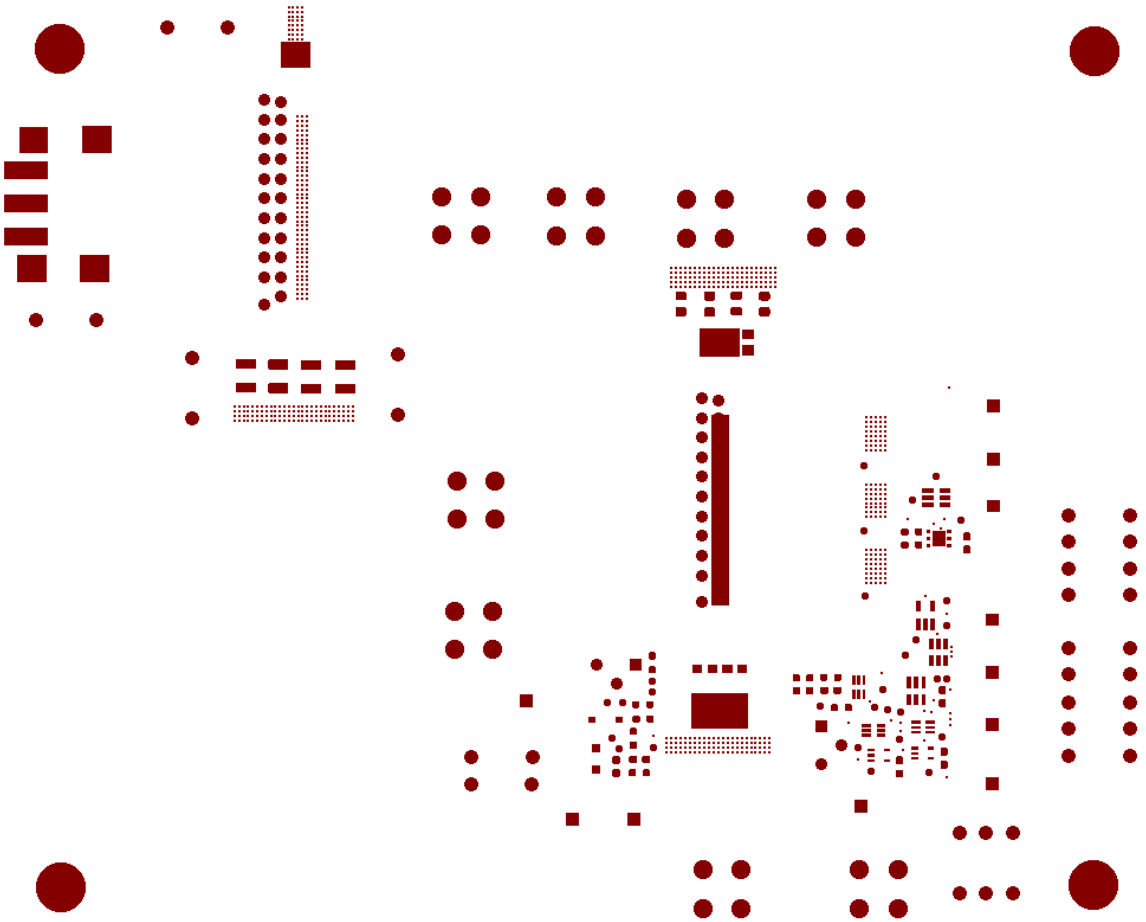

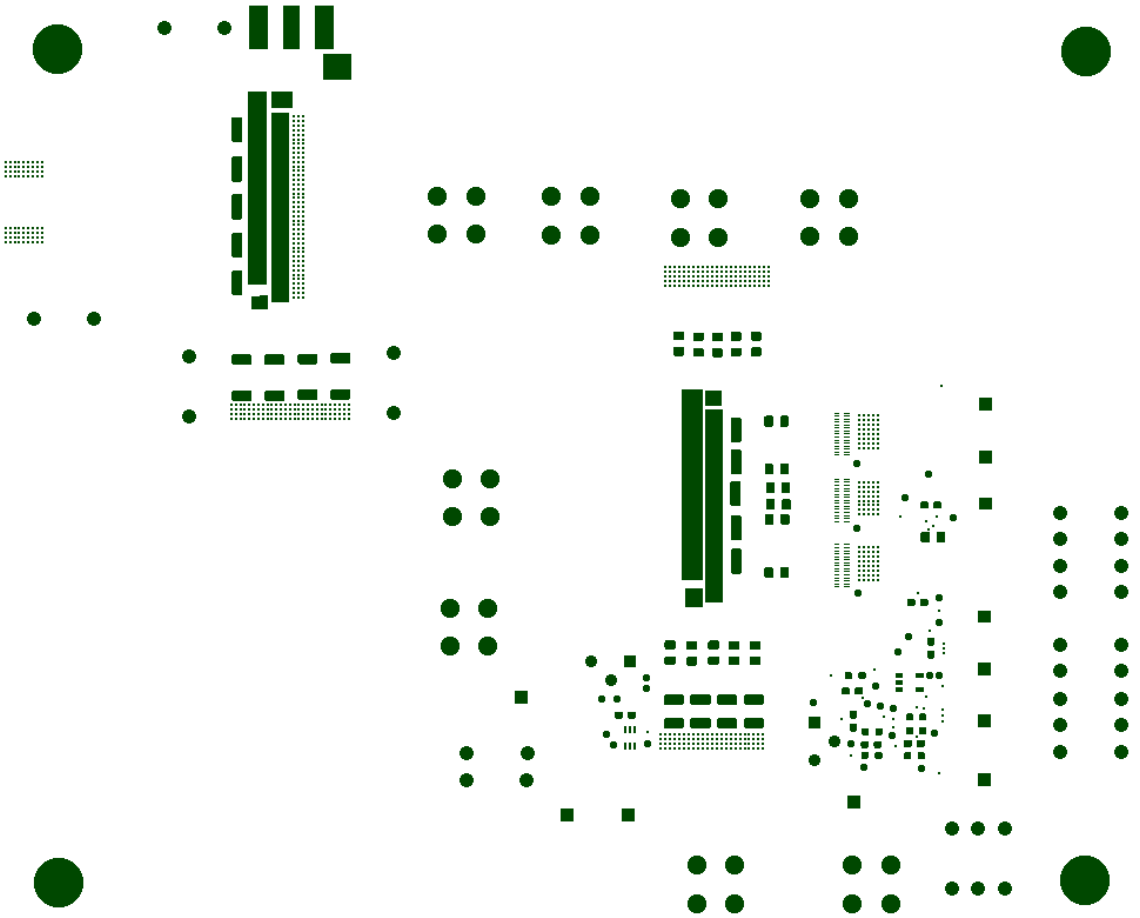

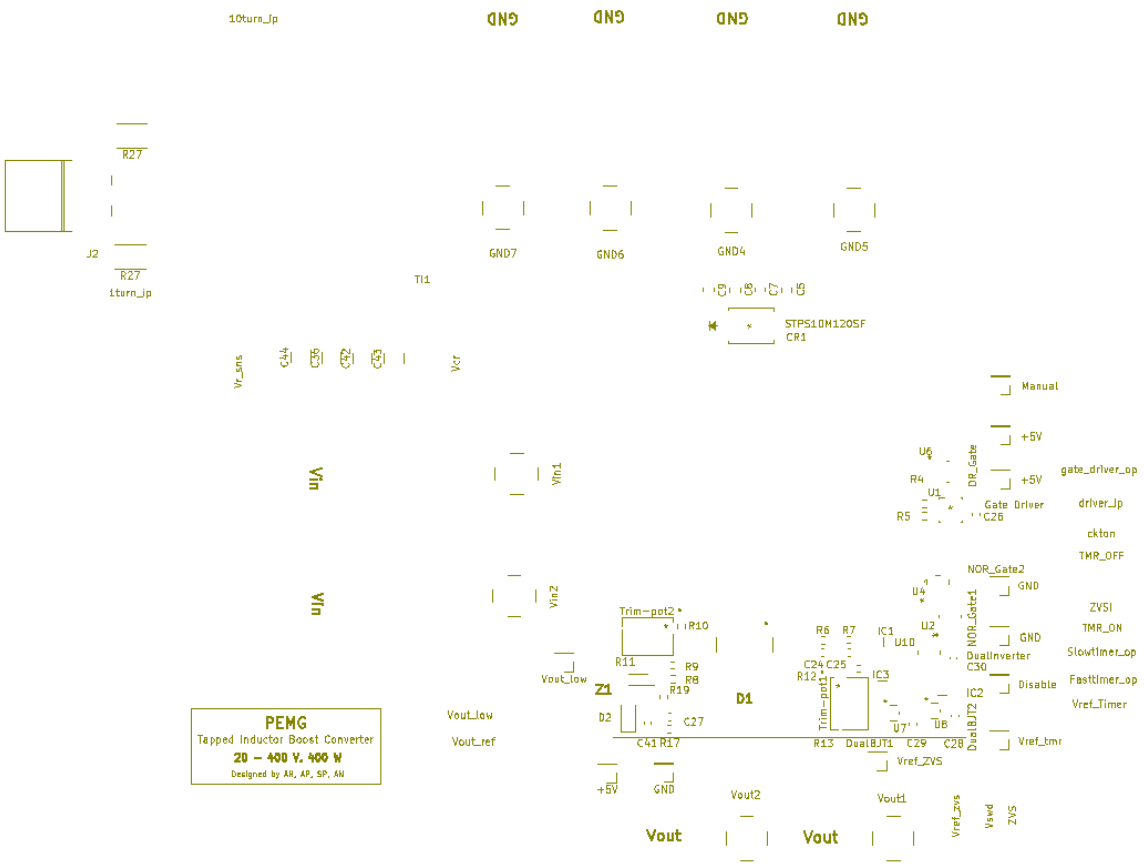
10turn_Ip
GND
GND
GND
GND
R27
J2
R27
iturn_Ip
GND7
GND6
GND4
GND5
T1
C9
C8
C7
C6
STPS10M120SF
CR1
Vr_sns
C44
C35
C42
C43
Vcr
Manual
+5V
+5V
gate_driver_op
U6
DR_Gate
R4
U1
R5
Gate Driver
C26
driver_Ip
ckton
TMR_OFF
NOR_Gate2
GND
ZVSI
TMR_ON
Slowtimer_op
Fasttimer_op
Vref_Timer
Vin
Vin
Vin1
Vin2
U4
NOR_Gate1
U2
IC1
U10
GND
DualInverter
C30
Disable
IC2
Trim-pot2
R10
R6
R7
C24
C25
R12
IC3
R11
R9
R8
R19
Z1
D1
Vout_low
Trim-pot1
D2
C27
U7
U8
DualBJT2
Vref_tmr
C41
R17
R13
DualBJT1
C29
C28
Vref_ZVS
Vout_low
Vout_ref
+5V
GND
Vout2
Vout1
Vout
Vout
Vref_zvs
Vswd
ZVS
PEMG
Tapped Inductor Boost Converter
20 – 400 V, 400 W
Designed by AH, AP, SP, AN

T7
R18
R22
R23
R24
R25
R31
R32
R33
R34
C4
C5
C6
C7
C8
C9
C10
C11
C12
C13
C14
C15
C16
C17
C18
C19
C20
C21
C22
C23
C24
C25
C26
C27
C28
C29
C30
C31
C32
C33
C34
C35
C36
C37
C38
C39
C40
R1
R2
R3
R4
R5
R6
R7
R8
R9
R10
R11
R12
R13
R14
R15
R16
R17
R19
R20
R21
Q1
Q2
Q3
Q4
D1
D2
D3
D4
D5
D6
D7
D8
D9
D10
D11
D12
D13
D14
D15
D16
D17
D18
D19
D20
D21
D22
D23
D24
D25
D26
D27
D28
D29
D30
D31
D32
D33
D34
D35
D36
D37
D38
D39
D40

# Bibliography


[1] Sullivan, Charles R., et al. "On size and magnetics: Why small efficient power inductors are rare." *2016 International Symposium on 3D Power Electronics Integration and Manufacturing (3D-PEIM)*. IEEE, 2016.

[2] Hu, Jiankun, and Charles R. Sullivan. "The quasi-distributed gap technique for planar inductors: Design guidelines." *IAS'97. Conference Record of the 1997 IEEE Industry Applications Conference Thirty-Second IAS Annual Meeting*. Vol. 2. IEEE, 1997.

[3] "Distributed air gaps in ferrite cores," EPCOS AG - a TDK Group Company,Tech. Rep., June 2017. [Online]. Available: https://de.tdk.eu/download/2113422/321697054fce0c768ea66959fde3b3db/ferrites-air-gaps-pb.pdf

[4] Spreen, James H. "Electrical terminal representation of conductor loss in transformers." *IEEE Transactions on Power Electronics* 5.4 (1990): 424-429.

[5] Tamyurek, Bunyamin, and David A. Torrey. "A three-phase unity power factor single-stage AC–DC converter based on an interleaved flyback topology." *IEEE transactions on Power Electronics* 26.1 (2010): 308-318.

[6] Tamyurek, Bunyamin, and Bilgehan Kirimer. "An interleaved high-power flyback inverter for photovoltaic applications." *IEEE transactions on Power Electronics* 30.6 (2014): 3228-3241.

[7] Yang, Rachel S., et al. "A low-loss inductor structure and design guidelines for high-frequency applications." *IEEE Transactions on Power Electronics* 34.10 (2019): 9993-10005.

[8] Balakrishnan, Arun, William T. Joines, and Thomas G. Wilson. "Air-gap reluctance and inductance calculations for magnetic circuits using a Schwarz-Christoffel transformation." *IEEE Transactions on Power Electronics* 12.4 (1997): 654-663.

[9] Hoke, Anderson F., and Charles R. Sullivan. "An improved two-dimensional numerical modeling method for E-core transformers." *APEC. Seventeenth Annual IEEE Applied Power Electronics Conference and Exposition (Cat. No. 02CH37335)*. Vol. 1. IEEE, 2002.

[10] Hanson, Alex J., et al. "Measurements and performance factor comparisons of magnetic materials at high frequency." *IEEE Transactions on Power Electronics* 31.11 (2016): 7909-7925.

[11] "High Frequency Power Materials," Fair-Rite Products Corp. [Online]. Available: https://www.fair-rite.com/wp-content/uploads/2018/02/HFPowerFlyer.pdf

[12] "Magnet wire, 17 AWG, Heavy Build, Enameled Copper," Remington Industries. [Online]. Available: https://www.remingtonindustries.com/magnet-wire/magnet-wire-17-awg-heavy-build-enameled-copper-6-spool-sizes/

[13] Foo, Benedict X., Aaron LF Stein, and Charles R. Sullivan. "A step-by-step guide to extracting winding resistance from an impedance measurement." *2017 IEEE Applied Power Electronics Conference and Exposition (APEC)*. IEEE, 2017.

[14] Li, Jieli, Tarek Abdallah, and Charles R. Sullivan. "Improved calculation of core loss with nonsinusoidal waveforms." *Conference Record of the 2001 IEEE Industry Applications Conference. 36th IAS Annual Meeting (Cat. No. 01CH37248)*. Vol. 4. IEEE, 2001.

[15] Venkatachalam, Kapil, et al. "Accurate prediction of ferrite core loss with nonsinusoidal waveforms using only Steinmetz parameters." *2002 IEEE Workshop on Computers in Power Electronics, 2002. Proceedings.*. IEEE, 2002.

[16] "3F46 Material Specification," Ferroxcube – A Yageo Company. [Online]. Available: https://www.ferroxcube.com/upload/media/product/file/MDS/3f46.pdf

[17] Sullivan, Charles R. "Layered foil as an alternative to litz wire: Multiple methods for equal current sharing among layers." *2014 IEEE 15th Workshop on Control and Modeling for Power Electronics (COMPEL)*. IEEE, 2014.

[18] Ouyang, Ziwei, Ole C. Thomsen, and Michael AE Andersen. "The analysis and comparison of leakage inductance in different winding arrangements for planar transformer." *2009 International Conference on Power Electronics and Drive Systems (PEDS)*. IEEE, 2009.

[19] Hanson, Alex J., and David J. Perreault. "Modeling the magnetic behavior of n-winding components: Approaches for unshackling switching superheroes." *IEEE Power Electronics Magazine* 7.1 (2020): 35-45.

[20] Han, Yongtao, and Yan-Fei Liu. "A practical transformer core loss measurement scheme for high-frequency power converter." *IEEE Transactions on Industrial Electronics* 55.2 (2008): 941-948.

[21] Foo, Benedict X., Aaron LF Stein, and Charles R. Sullivan. "A step-by-step guide to extracting winding resistance from an impedance measurement." *2017 IEEE Applied Power Electronics Conference and Exposition (APEC)*. IEEE, 2017.

[22] Han, Yehui, et al. "Evaluation of magnetic materials for very high frequency power applications." *IEEE Transactions on Power Electronics* 27.1 (2011): 425-435.

[23] Mu, Mingkai, et al. "New core loss measurement method for high-frequency magnetic materials." *IEEE Transactions on Power Electronics* 29.8 (2013): 4374-4381.

[24] Yang, Rachel S., et al. "Application Flexibility of a Low-Loss High-Frequency Inductor Structure." *2020 IEEE Applied Power Electronics Conference and Exposition (APEC)*. IEEE, 2020

[25] Liu, Yu-Chen, et al. "Design and Implementation of a Planar Transformer with Fractional Turns for High Power Density LLC Resonant Converters." *IEEE Transactions on Power Electronics* (2020).

[26] Iyer, Kartik V., William P. Robbins, and Ned Mohan. "Design and comparison of high frequency transformers using foil and round windings." *2014 International Power Electronics Conference (IPEC-Hiroshima 2014-ECCE ASIA)*. IEEE, 2014.

[27] Rahrovi, Babak, Ramin Tafazzoli Mehrjardi, and Mehrdad Ehsani. "On the Analysis and Design of High-Frequency Transformers for Dual and Triple Active Bridge Converters in More Electric Aircraft." *2021 IEEE Texas Power and Energy Conference (TPEC)*. IEEE, 2021.

[28] El Shafei, Ahmad, et al. "A High power high frequency transformer design for solid state transformer applications." *2019 8th International Conference on Renewable Energy Research and Applications (ICRERA)*. IEEE, 2019.

[29] Bal, Selva, Tuğçe Demirdelen, and Mehmet Tümay. "Three-Phase Distribution Transformer Modeling and Electromagnetic Transient Analysis Using ANSYS

Maxwell." *2019 3rd International Symposium on Multidisciplinary Studies and Innovative Technologies (ISMSIT)*. IEEE, 2019.

[30] Tikhonova, O., I. Malygin, and A. Plastun. "Calculation of Inductive Resistances of Induction Motor with Ring Windings by “ANSYS Maxwell”." *2018 International Conference on Industrial Engineering, Applications and Manufacturing (ICIEAM)*. IEEE, 2018.

[31] Tikhonova, Olga, et al. "Loss calculation of induction motor with ring windings by “ANSYS Maxwell”." *Актуальные проблемы электромеханики и электротехнологий АПЭЭТ-2017.—Екатеринбург, 2017* (2017): 63-66.

[32] Soria, Denisse A. Meza, Satish Ranade, and Olga Lavrova. "Exploring the Leakage Inductance of Transformers Used in Dual Active Bridge." *2019 North American Power Symposium (NAPS)*. IEEE, 2019.

[33] Iyer, K. V., et al. "A half-turn winding for compact, high-current, high-turns-ratio, low-leakage-inductance transformer." *2017 IEEE Energy Conversion Congress and Exposition (ECCE)*. IEEE, 2017.